ACS Catalysis

pubs.acs.org/acscatalysis

Research Article

Dynamics at Polarized Carbon Dioxide–Iron Oxyhydroxide Interfaces Unveil the Origin of Multicarbon Product Formation

Rosa Arrigo,* Raoul Blume, Verena Streibel, Chiara Genovese, Alberto Roldan,* Manfred E. Schuster, Claudio Ampelli, Siglinda Perathoner, Juan J. Velasco Vélez, Michael Hävecker, Axel Knop-Gericke, Robert Schlögl, and Gabriele Centi

Cite This: *ACS Catal.* 2022, 12, 411–430

Read Online

ACCESS | Metrics & More | Article Recommendations | Supporting Information

ABSTRACT: Surface-sensitive ambient pressure X-ray photoelectron spectroscopy and near-edge X-ray absorption fine structure spectroscopy combined with an electrocatalytic reactivity study, multilength-scale electron microscopy, and theoretical modeling provide insights into the gas-phase selective reduction of carbon dioxide to isopropanol on a nitrogen-doped carbon-supported iron oxyhydroxide electrocatalyst. Dissolved atomic carbon forms at relevant potentials for carbon dioxide reduction from the reduction of carbon monoxide chemisorbed on the surface of the ferrihydrite-like phase. Theoretical modeling reveals that the ferrihydrite structure allows vicinal chemisorbed carbon monoxide in the appropriate geometrical arrangement for coupling. Based on our observations, we suggest a mechanism of three-carbon-atom product formation, which involves the intermediate formation of atomic carbon that undergoes hydrogenation in the presence of hydrogen cations upon cathodic polarization. This mechanism is effective only in the case of thin ferrihydrite-like nanostructures coordinated at the edge planes of the graphitic support, where nitrogen edge sites stabilize these species and lower the overpotential for the reaction. Larger ferrihydrite-like nanoparticles are ineffective for electron transport.

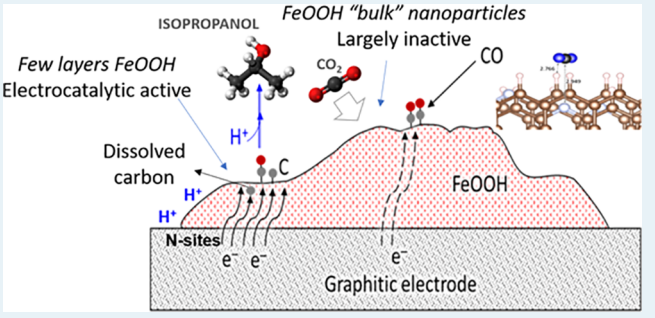

KEYWORDS: *N-doping, XPS, CO_2RR, Fe oxyhydroxide, C−C coupling*

INTRODUCTION

The electrocatalytic conversion of CO_2 to chemicals and fuels is currently one of the challenging frontiers of research from both application and fundamental perspectives.[1] While earlier studies focused on the production of C_1 compounds, there has been increased interest in the direct formation of higher-added-value C_{2+} products (compounds with more than two carbon atoms).[2]

Earlier studies on the electrocatalytic CO_2 reduction reaction (CO_2RR) evidenced the unique ability of Cu to form several hydrocarbons and alcohols.[3−8] Forming multicarbon products in a selective fashion is, however, technically challenging because it requires a multielectron transfer reaction coupled with the formation of C−C bonds.[3] Many contributions have focused on maximizing productivities toward C−C coupling products,[9] and numerous studies have analyzed the mechanism of multicarbon product formation in the CO_2RR with the aim of unravelling catalyst design strategies for the selective reduction.[9−27] Still, contrasting opinions exist, mainly on the three following points:

1. Is nanostructured metallic Cu exclusively required for C_{2+} product formation or can these products also form starting from nonmetallic nanoparticles (such as oxides and hydroxides) of other transition metals?
2. Do the reaction paths leading to C_{2+} products have to involve surface coupling reactions between specific chemisorbed species? Currently, C_2 products are described as being formed from the dimerization of two chemisorbed CO molecules,[26] the coupling of chemisorbed CO with other intermediates such as CHO[11] and other C_2 intermediates,[13] or the coupling of surface adsorbates other than CO.[14]
3. Which other factors will determine the occurrence of C−C bond formation? Nanoconfinement,[16−18] surface strains,[21] and the creation of a fractal dimension at the nanoscale[22] were indicated to facilitate the C−C coupling together with mesoscale conditions that forced

Received: September 18, 2021
Revised: November 22, 2021

https://doi.org/10.1021/acscatal.1c04296
ACS Catal. 2022, 12, 411−430

a higher surface concentration of CO_2-derived adspecies.[7,19]

Increased evidence suggests that a complex interplay of many factors determines the occurrence of C−C bond formation, including the surface structure (at the nano and mesoscale), the specific reaction conditions (pH, buffer strength, and ion effects), and mass-transport-related effects.[2] Indeed, these interrelations should be borne in mind when turning to alternative systems for CO_2 reduction.

In this work, we focus on the mechanism of multicarbon product formation on electrocatalytic systems beyond Cu, namely Fe oxyhydroxide systems. Centi et al.[28] showed experimentally that isopropanol can be formed on a metal oxide system such as iron oxide supported on carbon nanotubes via a gas-phase CO_2RR, using a polymeric proton exchange membrane in direct contact with the electrocatalyst on one side. On the other side, the electrocatalyst is in direct contact with CO_2 gas molecules. The scope of the electrocatalytic gas-phase approach is to enhance the CO_2 surface coverage of the electrocatalyst; in a liquid electrolyte, this is limited by both the CO_2 solubility in the electrolyte and the transport across the electrical double layer.

By using C-supported Fe catalytic systems, we showed that a controlled surface chemical modification of the carbon support by O or N enables the tuning of the electrocatalytic performance and realizes high Faraday efficiencies and selectivities toward C_2 and C_{2+} products both in the liquid phase[6] and in gas-phase approaches,[29] respectively. In these Fe−N−C electrocatalysts, the defective N sites of the carbon support were shown to profoundly influence the energy of the specific CO_2 chemisorption sites on the Fe phase,[29] which is expected to affect the reaction pathways. Also, N-doping of the carbon support affects the spatial distribution of hydrophilic N sites and graphitic hydrophobic domains, which in turn have other effects relevant for CO_2 reduction such as the control of proton and solvent molecule availability at the reactive interphase.[29−31] The experimental conditions of the electroreduction (either in gas or in the liquid phase) also influence the CO_2 and H^+ availability at the cathodic electrocatalyst surface, whereas the nanostructure of the active phase determines not only the nature of the sites for specific CO_2 chemisorption but also the mechanism and kinetics of electron transfer. The interplay of these factors determines whether surface intermediates will undergo hydrogenation and desorption or successive coupling reactions that lead to heavier products. Due to the dynamic nature of the reactive interphase, an in-depth mechanistic study requires a combination of theoretical[32] and experimental approaches.[10,33−38]

The observation of selective C_3 chemistry on C-supported Fe-oxide electrocatalysts[28−31] under gas-phase conditions is relevant from both fundamental and applied chemistry perspectives. Therefore, it motivates further mechanistic studies using advanced surface-sensitive *in situ* spectroscopic methods to better understand the nature of the active interphase and its dynamic dependence on the experimental conditions during the CO_2 electrocatalytic reduction.

Particularly, ambient pressure X-ray photoelectron and near-edge X-ray absorption fine structure spectroscopies (APXPS and NEXAFS, respectively) have been proven to provide unparalleled resolution of chemical states at polarized electrode interfaces.[33−40] While operando X-ray spectroscopic studies applied to CO_2RR have focused on absorption spectroscopy at the metal edges,[10] APXPS remains unexplored in the CO_2RR, due to the challenges in realizing electron detection in wet environments. However, APXPS also enables the simultaneous monitoring of C and O interfacial species; consequently, it is the ideal technique to provide new insights into the mechanism of multicarbon product formation. Here, we report a comparative mechanistic study on the carbon dioxide reduction electrocatalysis of self-standing graphite-supported ferrihydrite-like-based electrocatalytic systems. We use electrocatalytic systems of a similar ferrihydrite-like structure, which are immobilized either on nitrogen-functionalized (FeOOH/NC) or oxygen-functionalized (FeOOH/OC) carbon paper. These systems are chemically identical to the electrocatalysts tested in the liquid-phase CO_2RR in ref 6 but differ from those tested in ref 29 in terms of the structure of the C support and the Fe speciation. We show that they are characterized by quite different electrocatalytic performances in the gas-phase CO_2 reduction in terms of isopropanol productivity and therefore are ideal for comparative mechanistic studies. APXPS and NEXAFS in combination with electroanalytical techniques such as chronoamperometry (CA) and cyclic voltammetry (CV) were used to identify surface and interfacial structural features formed under conditions of gas-phase carbon dioxide electroreduction. These dynamics are correlated to the electrocatalysts' performances, which were determined *in situ* by online gas detection via mass spectrometry.

Tailored *in situ* experiments enable us to close the experimental conditions gaps between *in situ* studies and catalyst performance screening at atmospheric pressure. Together with multilength-scale electron microscopy characterization and theoretical modeling, these results allow us to unveil the origin of C_3 formation in the CO_2RR over Fe-based electrocatalytic systems under gas-phase conditions. Hence, we provide a framework to guide improvements in material developments for CO_2 reduction from a fundamental perspective.

EXPERIMENTAL SECTION

Sample Preparation. The preparation of the electrocatalysts was previously reported.[6,41] Briefly, TorayTM carbon paper TGP-H-030 (FuelCellStore.com) with a thickness of 0.1 mm was cut into pieces of approximately 0.8 × 0.8 cm^2 (approximately 4.2 mg) and used as a support for the iron oxide particles. Prior to the metal precursor impregnation, the carbon paper was functionalized with either O or N groups, adapting the procedure from Arrigo et al.[42,43] This preparation procedure has the following advantages: (a) easy assembly in the *in situ* electrochemical cell and (b) no need to prepare an electrocatalyst ink, which could detach from the substrate surface into the solution with time. First, several pieces were heated to 393 K in HNO_3 (250 mL, 70% Sigma-Aldrich) for 4 h, followed by drying in static air overnight at 373 K. Oxygen functionalization with concentrated HNO_3 produces a hydrophilic carbon surface with mainly carboxylic functional groups.[42,44] Then, the HNO_3-treated samples were put in a tube furnace under 50 mL min^{-1} NH_3 (99.98% Ammonia Micrographic, BOC Linde) at 873 K for 4 h. Afterward, the samples were cooled to 323 K in NH_3 and further to RT in N_2 (50 mL min^{-1}, BOC Linde). The N-functionalization at 873 K in NH_3 produces a hydrophobic surface with mainly pyridine-like N species.[42−45]

The Fe-containing samples were obtained via the incipient wetness impregnation of an $Fe(NO_3)_3{\cdot}9H_2O$ solution in H_2O/

https://doi.org/10.1021/acscatal.1c04296
ACS Catal. 2022, 12, 411−430

ethanol (24:1). A 100 μL aliquot of a 3 g L^{-1} solution was used to prepare the 1 wt % samples, where the percentage refers to the weight expressed as metallic Fe. The solution was added dropwise to the N-functionalized cloth piece, making sure the wetting was quantitative and macroscopically homogeneous. The impregnated carbon paper pieces were dried at room temperature in static air overnight. Afterward, the samples were heated at 250 °C in N_2 (50 mL min-1, BOC Linde) for 3 h to achieve the decomposition of the metal precursor without decomposing the nitrogen species of the support. The samples were cooled to RT in N_2 and afterward exposed to air. This sample is referred to here as FeOOH/NC. The same impregnation procedure was used for the O-functionalized carbon paper (O−C) to prepare a control sample, namely FeOOH/OC. If not otherwise stated, the nominal sample loading is always 1 wt % of metallic iron. The elemental compositions for the two samples as determined by XPS are reported in Table S1. Another sample was obtained by subjecting the FeOOH/NC to a thermal annealing in the *in situ* XPS chamber under UHV conditions at 473 K. This sample is referred herein to as T-FeOOH/NC.

Electrocatalytic Tests in a Gas-Phase Electrochemical Cell. Tests of CO_2 gas-phase reduction (CO_2GR) were conducted at room temperature in a flow electrocatalytic cell operating the CO_2 electrocatalytic reduction in the absence of a liquid electrolyte at the cathode side, which is thus defined as gas-phase electrochemical cell (GPEC) operation.[30,31] Note, however, that the membrane in contact with the electrocatalysts acts as solid electrolyte to close the circuit. These gas-phase operations allow us to maximize the formation of C_{2+} products.[29−31] The working electrode (WE) was assembled by hot-pressing the TorayTM carbon paper-based electrodes onto a selective proton exchange membrane (Nafion 117, supplied by Ion Power) at 80 atm and 120 °C for 60 s. The WE (a gas-diffusion layer (GDL)-type electrode) was in direct contact with pure CO_2. The electrode had a diameter of about 3 cm^2. The cell had a three-electrode configuration, with a platinum wire as counter electrode (CE) and a 3 M Ag/AgCl electrode as a reference electrode (RE). The cell operated at ambient pressure and temperature. The cell (in the cathodic part) was adapted to have closer characteristics to those used in operando tests, where the electrocatalyst (with a size about 0.8 × 0.8 cm^2) was put on a larger GDL piece (around 7 cm^2). The GDL is not inert toward H_2 formation and thus its contribution was subtracted. The cell is divided in two compartments by the solid electrolyte membrane hot-pressed with the WE. The CE and RE were immersed in an aqueous electrolyte solution (0.5 M $KHCO_3$) in one of the compartments facing the polymeric electrolyte membrane side of the membrane−WE assembly (MEA), namely the WE side of the MEA is in the gas-phase compartment. The electrolyte solution provides the protons needed for the reduction, which diffuse to the WE catalyst through the Nafion membrane. A potentiostat and galvanostat (Amel mod. 2049A) was used to supply a constant voltage at the WE (in the range from −0.5 to −1.5 V vs Ag/AgCl) to supply the electrons necessary for the CO_2 reduction process. At the end of the reaction (1 h if not otherwise indicated), the polarity was inverted for two seconds to facilitate the desorption of the products from the WE without further oxidizing the products. The liquid products were collected in a cold trap and analyzed by a gas chromatograph equipped with a mass spectrometer (Thermo Scientific GC-MS, Trace 1310GC-TSQ8000EVO, Triple Quadrupole MS, Stabilwax column). An internal standard was used to minimize errors in quantification.

A systematic comparative quantitative analysis by GC-MS and NMR was performed on the sampled solutions, with the better reproducibility of the former method showing an average error of less than 5%. The results of the GC-MS analysis are therefore used to present the electrocatalytic tests, which refer to the average behavior observed in 1 h of operation. The gas products were detected by sampling the gaseous stream leaving the external container at regular intervals and analyzing samples by gas-chromatography (GC-TCD, Agilent 7890A, 5A Plot column).

Isotopic labeling tests were performed over tge FeOOH/NC sample at −1.0 V vs Ag/AgCl under the same conditions and using the same electrochemical cell and GC-MS but by feeding $^{13}CO_2$ (99.0 atom % ^{13}C CO_2, Sigma-Aldrich) into the gas cathodic chamber and using aqueous 0.5 M $KH^{13}CO_3$ (98 atom % ^{13}C, Sigma-Aldrich) as the liquid anolyte. The Faraday efficiency (FE) was calculated according to eq 1 as follows:

$$FE(\%) = e_{out}/e_{in} \times 100 \quad (1)$$

where in $e_{in} = Q/F$, F is the Faraday constant (96485 C mol^{-1}), Q is the measured charge according to $Q = I \times t$, I is the current, and t is time. e_{out} is mol product × n, where n is the number of electrons required to reduce CO_2 to a particular product and the moles of products were quantified by GC. Background contribution of the support GDL was subtracted.

***In Situ* Electrochemical Flow Cell (ISEC).** A three-electrode electrochemical flow cell designed for the APXPS end-station of the ISISS beamline at BESSY II/HZB was used for *in situ* spectroscopy (Figure 1). This technique allows the analysis of the electronic structure of the electrical double layer formed upon polarization at the electrode interfaces.[34−40] It is

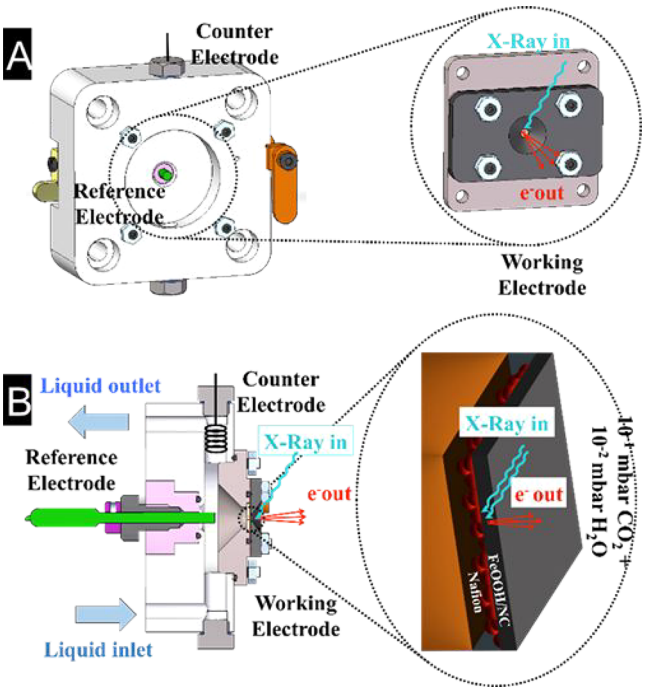

Figure 1. *In situ* electrochemical cell (ISEC) for ambient-pressure XPS. (a) Front view showing the mounting of the lid composed of two plates that host the WE. (b) Side view showing the arrangement of the three electrodes and the membrane electrode assembly.

https://doi.org/10.1021/acscatal.1c04296
ACS Catal. 2022, 12, 411−430

thus well-suited to characterize operando conditions that lead to multicarbon product formation during CO_2 electrocatalytic reduction. Details on the cell were given previously.[36,37,39]

For the studies reported here, we used a cell configuration in which the CE (Pt wire) and the RE (Ag/AgCl (3M), DRIREF-2SH, World Precision Instruments) were immersed in a liquid electrolyte (0.05 M H_2SO_4) that flowed continuously through the cell. The CE and the RE immersed into the electrolyte stream were separated from the evacuated XPS measurement chamber of the end station by a sandwiched membrane electrode assembly (MEA) based on a Nafion 117 PEM (Alfa Aeser), which previously was purified from organic contaminants and then activated as described in ref 36. In this case, the PEM serves also to prevent the liquid electrolyte from entering the measurement chamber and hence guarantees the leak-tightness of the *in situ* cell.

The WE of this MEA consists of carbon paper, previously treated as described in the sample preparation section, sandwiched between the polymeric electrolyte membrane and the lid of the *in situ* cell. To preserve leak-tightness, no hot-pressing treatment of the WE and the PEM was applied in this part of the study. The water-based electrolyte hydrates the polymeric electrolyte membrane (PEM), ensuring ion conductivity. Through this hydration, water molecules are transferred into the evacuated measurement chamber, generating an equilibrium water pressure ranging between 0.05 and 0.09 mbar. To this atmosphere, a constant flow of 3 mL min^{-1} CO_2 (99.995%) corresponding to a measured pressure of 0.09 mbar was added to the chamber using a mass flow controller to achieve a total pressure of 0.15−0.18 mbar. A potentiostat (SP-300, Bio-Logic Science Instruments SAS, France) controlled the potential of the WE with respect to the RE and measured the current between the CE and the WE. Here we chose to ground the WE to the electron analyzer to prevent shifts of the core levels due to the applied potential. A quadrupole mass spectrometer (QMS) monitored the gas composition online in the XPS chamber.

Analysis of the Electrocatalytic Performances during *In Situ* Experiments. With the setup described above, XPS and NEXAFS spectra of the X-ray-exposed WE were recorded at different constant voltages versus the Ag/AgCl RE. Before the spectroscopic measurements, four cycles of cyclic voltammetry (50 mV s^{-1}) were performed first under the water partial pressure generated by the transport of the electrolyte through the membrane and then after adding a constant flow of CO_2 to this atmosphere equivalent to a partial pressure of 0.9 mbar CO_2 in the analysis chamber. During the measurements at constant voltage (chronoamperometry measurements) as well as the potential sweep (cyclic voltammetry), the value of the current exchanged was monitored together with the total pressure in the XPS chamber, and the gas phase was analyzed via MS to evaluate the performances of the electrocatalysts. The mass fragments m/z 2, 12, 14, 15, 16, 17, 18, 28, 30, 32, 34, 44, 45, 46, and 60 were monitored in each *in situ* experiment. In the case of the CV, the analysis involves the evaluation of the m/z 2 peak area, representing the H_2 evolved per cycle as a function of the charge exchanged during each voltammetry cycle. The m/z 2 peak area was obtained by integrating the peak related to each cycle in the mass spectrum after linear background subtraction. Similarly, the charge exchanged per cycle was obtained by integrating the relative peak in the current (I) versus time plot of the CV. For the CA experiments, the cumulative charge measured was evaluated as a function of the H_2 efficiency parameter (HEP). The HEP is given by eq 2 as follows:

$$\mathrm{HEP} = (n \cdot \mathrm{AH}_2 \cdot F)/Q \quad (2)$$

where n is the number of electrons exchanged; in the case of H_2, this is 2. AH_2 is the area of m/z 2 representing the amount of H_2 evolved during the constant potential experiment, F is the Faraday constant, and Q is the total charge exchanged during the constant potential experiment, which was obtained by integrating the relative area in the current versus time plot.

***In Situ* XPS and NEXAFS.** XPS measurements were performed by applying a suitable excitation energy, which corresponded to the kinetic energy (KE) of the photoemitted electrons as indicated in each case for the core levels Fe 2p, C 1s, O 1s, and N 1s. The pass energy (E_p) was set to 20 eV. The spectra were collected with a spot size of ≈150 μm × 80 μm. The beamline settings were an exit slit (ES) of 111 μm and a fix focus constant (cff) of 2.25.

Auger electron yield (AEY) NEXAFS spectra were recorded with an analyzer setting of E_p = 50 eV and electron kinetic energies (KE) of 700, 350, and 240 eV for the Fe L-edge, N K-edge, and C K-edge, respectively. The beamline settings were an exit slit (ES) of 111 μm and a fix focus constant (cff) of 1.4. The kinetic energy windows were chosen so as to avoid contribution from other photoelectric processes to the NEXAFS spectra in the excitation energy window used. The rather high E_p was necessary to obtain a reasonable intensity. The exit slit value chosen allowed an optimal compromise between a high photon intensity and a good spectral resolution. The higher order suppression operation mode of the monochromator (cff = 1.4) was applied to avoid contributions to the background in the NEXAFS spectra that might complicate intensity normalization of the spectra on the impinging photon flux.

XPS Fitting. A fitting procedure was developed that described the surface changes of the Fe phase and the O and C species upon CO_2 electroreduction during the *in situ* characterization. The photoelectron binding energy (BE) is referenced to the Fermi edge when possible. In all other cases, BEs were referenced to the maximum of the C 1s core level peak (284.32 eV) measured after each core level measurement at the corresponding excitation energy.

The Fe 2p, C 1s, and O 1s spectra were fitted following the Levenberg−Marquardt algorithm to minimize χ^2. Peak shapes were modeled using Doniach−Sunjic functions convoluted with Gaussian profiles to consistently describe chemical and structural changes among the samples and upon the different *in situ* conditions investigated.[46] Background correction was performed using a Shirley background.[47] The peak area ratio between the Fe $2p_{3/2}$ and Fe $2p_{1/2}$ spin orbit split transitions was constrained approximately to the theoretical value of 2:1. The accuracy of the fitted peak positions is ≈0.05 eV. The full-width at half-maximum (fwhm) values of the peaks were constrained during the fitting. The C 1s XPS spectra were fitted using the fitting model reported by Blume et al.[48] The assignment of the components in the C 1s XPS spectra is given in Table 1.

The analysis of the Fe 2p XPS spectra for a multicomponent oxide is complicated due to the multiplet structure of the overlapping core-level peaks and satellites for the many phases present.

In this work, the entire Fe 2p XPS core level was fitted using the approach reported by Biesinger et al.[49] that, beside

https://doi.org/10.1021/acscatal.1c04296
ACS Catal. 2022, 12, 411−430

Table 1. Assignment of C 1s Components Based on the Fitting Described in Referece 48

label	binding energy (BE) (eV)	assignment	fwhm
C0	283.6	dissolved C	0.6
C1	284.0	defective sp^2 carbon	0.6
C2	284.3	graphitic sp^2 carbon	0.5
C3	284.6−284.8	disordered carbon (accounts for larger holes in basal graphitic planes, nonsaturated bonds, and the amorphous carbon phase)	0.65
C4	285.2	sp^3 C−H bonds	0.6
C5	285.5 and higher	C−O bonds	1.1

regarding the chemical states, includes features caused by multiplet splitting and shake-up processes of plasmon losses. The peak assignments are listed in Table 2.

Table 2. Assignment of Fe $2p_{3/2}$ Components Based on the Fitting Described in Reference 49

label	binding energy (BE) (eV)	assignment	fwhm
Fe0	706.9	Fe metal	1.5
Fe1	708.5	Fe(II)−O in wüstite (FeO) Fe(III)−O in hematite	1.7
Fe2	709.8	(Fe_2O_3) or Fe(II)−O in FeO	1.9−2.0
Fe3	710.3	Fe(III)−O in oxyhydroxides (FeOOH)	1.7
Fe4	710.8	Fe(III)−O in hematite or the Fe(II)−O bond in FeO	1.8−2.0
Fe5	711.5	Fe(III)−OH in Fe_2O_3 and FeOOH	1.6−2.0
Fe6	712.2	Fe(II/III)−OH in Fe_3O_4, FeO, and FeOOH	1.7−3.0
Fe7	713.5	Fe(III)−OH in Fe_2O_3 and FeOOH	2.0−2.5
Fe8	714−715.7	Fe(II)-dominated satellites	3.6−3.8
Fe9	719	Fe(III) satellites	2.0−3.9

Similarly, the analysis of the O 1s spectra was complicated by the fact that the oxygen species belong to both the Fe phases and the C support as well as to chemisorbed water and CO_2-related species. In this work the O 1s spectra were fitted[50] as described in Table 3.

Table 3. Assignment of O 1s Components from Reference 50

label	binding energy (BE) (eV)	assignment	fwhm
O1	529.6	Fe(III)−O	0.85
O2	530	Fe(III)−O	0.85
O3	530.3	Carbonyl C═O/Fe(II)−O	1.3
O4	531.1	Lactone C═O/Fe−OH	1.3
O5	531.9	carboxyl	1.3
O6	532.7	anhydride ether	1.3
O7	533.4	lactone ether	1.3
O8	534.4	O−H bonds	1.3

Due to the complex analysis of these Fe systems, the fitting procedure was validated against an *in situ* temperature-programmed XPS study of the fresh FeOOH/NC electrocatalyst, for which structural transformations involving the Fe phase were previously investigated using transmission electron crystallography.[41] This approach proved to be very useful for developing a consistent fitting procedure that described structural transformation involving the Fe phase. The experiment is described in detail in the Supporting Information together with the relative C 1s, Fe 2p, and O 1s XPS core-level spectra. Derived peaks intensities trends are shown in Supplementary Figures S1, S2, S3, and S4, respectively.

Moreover, due to the many overlapping peaks belonging to the different phases, peaks with a peak maximum falling at a very close BE were merged. A scheme that clarifies this approach is reported in Supplementary Figure S2b.

Electron Microscopy Techniques. Bright field (BF) and high-angle annular dark field scanning transmission electron microscopy (HAADF STEM) images were acquired with a probe-corrected ARM200F at the ePSIC facility (Diamond Light Source) with an acceleration voltage of 200 keV. Measurement conditions were a CL aperture of 30 μm, a convergence semiangle of 24.3 mrad, a beam current of 12 pA, and scattering angles of 0−10 and 35−110 mrad for BF and HAADF STEM, respectively. Scanning electron microscopy (SEM) analyses were performed on a Zeiss Ultra SEM operating at acceleration voltages of 1.6 and 20 keV.

Computational Methods. We created a computational model of the CO_2 reduction process on the ferrihydrite-like layer on pristine and nitrogen-doped graphite (010) according to the experimental data. These calculations based on spin-polarized periodic plane-wave density functional theory (DFT) were performed with the Vienna *Ab Initio* Simulation Package (VASP).[51] The density functional of Perdew, Burke, and Ernzerhoff (PBE)[52] was used to calculate the exchange and correlation contributions. To describe long-range interactions, which are necessary to describe the interaction between molecules and solids,[53−55] we used the zero-damping Grimme's empirical dispersion correction (DFT-D3).[56]

The projector-augmented wave (PAW) formalism[57] as implemented in VASP was employed to describe the core electrons. A plane-wave kinetic cutoff was set at 550 eV. The Brillouin zone was sampled with a mesh of points separated by 0.2 $Å^{-1}$. Dipole corrections were applied perpendicular to the surfaces upon the adsorption of FeOOH on the C and N-doped C support (NC). Bader charges were calculated to assign partial charges to specific atoms.[58] The graphitic support (010) surface was modeled as a fully relaxed slab that was 12 atomic layers thick with two exposed graphene layers at the top and bottom, which were terminated with hydrogens for consistency. About 2% of the C atoms were substituted by nitrogen, simulating the NC. A FeOOH slab with an area of 88.99 $Å^2$ was supported and fully relaxed on the graphitic facet (Figure 2). A vacuum of 10 Å perpendicular to the surface ensured no spurious interaction with periodically repeated slabs. Table 4 reports the average distance of the model.

$$E_{Ads} = \frac{E_{Sys} - (E_s + E_{Mol})}{n} \quad (3)$$

The flexibility of the FeOOH layers is noticeable based on the variable distances between Fe atoms. We calculated the adsorption energies (E_{Ads}) from the total energy of the optimized structure of the molecule and the adsorbent (E_{Sys}), the energy of the optimized naked adsorbent, *i.e.*, FeOOH/C and FeOOH/NC (E_S), and the energy of the isolated molecule in the gas phase (E_{Mol}), respecting the total number of adsorbed molecules (n) (eq 3). Note, however, that in reality the graphitic support is more defective and the adsorption

https://doi.org/10.1021/acscatal.1c04296
ACS Catal. 2022, 12, 411−430

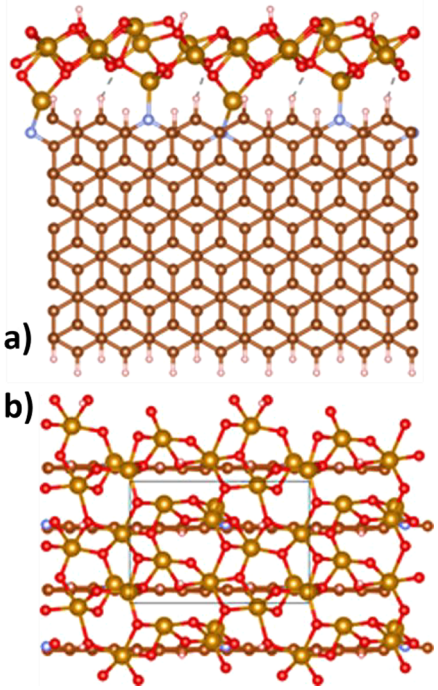

Figure 2. Schematic representations of an FeOOH-like thin film on N-doped graphite. (a and b) Top views and schematic representations of an FeOOH-like thin film on N-doped graphite. The black frame in the top view in panel b indicates the actual simulation cell. The color scheme for C, N, O, Fe, and H is brown, blue, red, dark yellow, and pink, respectively.

Table 4. Average Distances in the Supported FeOOH According to the DFT Model

	d(Fe−Fe) (Å)	d(Fe−O) (Å)	d(O−H) (Å)
FeOOH	2.775	1.863	0.989
FeOOH/C	2.036	1.948	0.977
FeOOH/NC	2.912	1.930	0.976

energy values will depend strongly on the distribution of these defective atoms.

RESULTS AND DISCUSSION

We adopted here an electrode preparation that was modified from ref 29 and adapted it to the *in situ* electrochemical cell; both processes are described in detail in the Experimental section. The electronic structure and quantitative elemental composition of the fresh samples investigated in this study were determined using a multitechnique approach.[6,41] In what follows, we describe the large particles as ferrihydrite-like nanostructures because their bulk-sensitive hard X-ray absorption fine structure spectroscopic characterization resembles the one reported for ferrihydrite; however, it must be noted that neither the 6-line nor the 2-line X-ray diffraction patterns were observed, which are typical for highly and poorly ordered ferrihydrite, respectively.[6]

We present the results of the nanostructural characterization of these ferrihydrite-like based electrodes by means of multilength-scale electron microscopy techniques, with particular emphasis on the thin films of the Fe oxyhydroxide phase covering the graphitic support; later on, we will show that these were found to be the electroactive species under the conditions investigated.

The adaptation of the electrocatalyst preparation to the *in situ* spectroscopic study using a self-standing electrode approach based on FeOOH-impregnated functionalized carbon paper required a confirmation of the expected trends in the electrocatalytic performance by a preliminary screening that used the same gas-phase electrochemical cell (GPEC) used in previous studies.[28−31] Therefore, the catalytic performances in the GPEC of these systems will be presented under the same voltages explored during the electrocatalytic *in situ* study. Subsequently, the electronic structure characterization of the surface and near-surface region of the electrode upon CO_2 electroreduction is presented and correlated to the electrocatalyst performances. Finally, a theoretical model of the interface will be presented to help rationalize our findings.

Electron Microscopy Characterization. The visual inspection of these materials by electron microscopy reveals a distribution of nanostructures of different nuclearity (Figure 3a and b), from large particles of irregular shape with the typical nanostructure observed for ferrihydrite[59] (Figure 3c) to low-dimensional films (Figure 3d−g) and atomically dispersed iron species or few-atom clusters. The scanning electron microscopy (SEM) characterizations of FeOOH/NC and FeOOH/OC at low- and high-acceleration voltages are reported in Supplementary Figure S5 and S6, respectively, and discussed in detail therein. We find that the large particles are mostly localized in the interspace region within the graphitic fibers of the carbon paper. Moreover, a rather homogeneously deposited Fe-containing thin film covers the fibers.

An example of large particles of irregular shape can be seen in the low-magnification scanning transmission electron microscopy (STEM) images in Figure 3b and Supplementary Figure S7 and in Figure 3a and Supplementary Figure S8 for FeOOH/NC and FeOOH/OC, respectively.

Supplementary Figure S9 shows high-angle annular scanning transmission electron micrographs in the S9a bright field (BF) and S9b dark field (DF) modes for FeOOH/NC visualized along the [001] zone axis of the graphite structure. There, it is possible to identify polynuclear Fe species and few-atom clusters, which are localized at the edges of the graphene layers composing the graphitic carbon structure.[6] We note that increasing the Fe loading produces larger particles in higher abundance; however, the structural features attributed to polynuclear or few atom FeOOH clusters were found as well (Supplementary Figure S10). Moreover, low-dimensional polynuclear FeOOH species not only decorate the edge terminations but also cover the basal planes, which can be seen in the low-magnification high-angle annular dark field scanning transmission electron microscopy (HAADF-STEM) images with relative elemental mapping images for FeOOH/OC and FeOOH/NC in Figure 3a and b, respectively.

A clearer picture of these low-dimensional polynuclear FeOOH species and their localization on the graphitic support is provided in Figure 3 d−g. Here, the edge planes of the graphitic structure of the support are visualized as well as the interfacial graphite−FeOOH thin film region of the FeOOH/NC sample.

The brighter areas in the HAADF-STEM images (Figure 3 d and g) correspond to the Fe-containing phase, being the contrast of this operation mode generated by high-angle scattered electrons and thus sensitive to the atomic number of the scatterer. Consistently, low-dimensional ferrihydrite-like nanostructures are present as patches of a rather irregular

https://doi.org/10.1021/acscatal.1c04296
ACS Catal. 2022, 12, 411−430

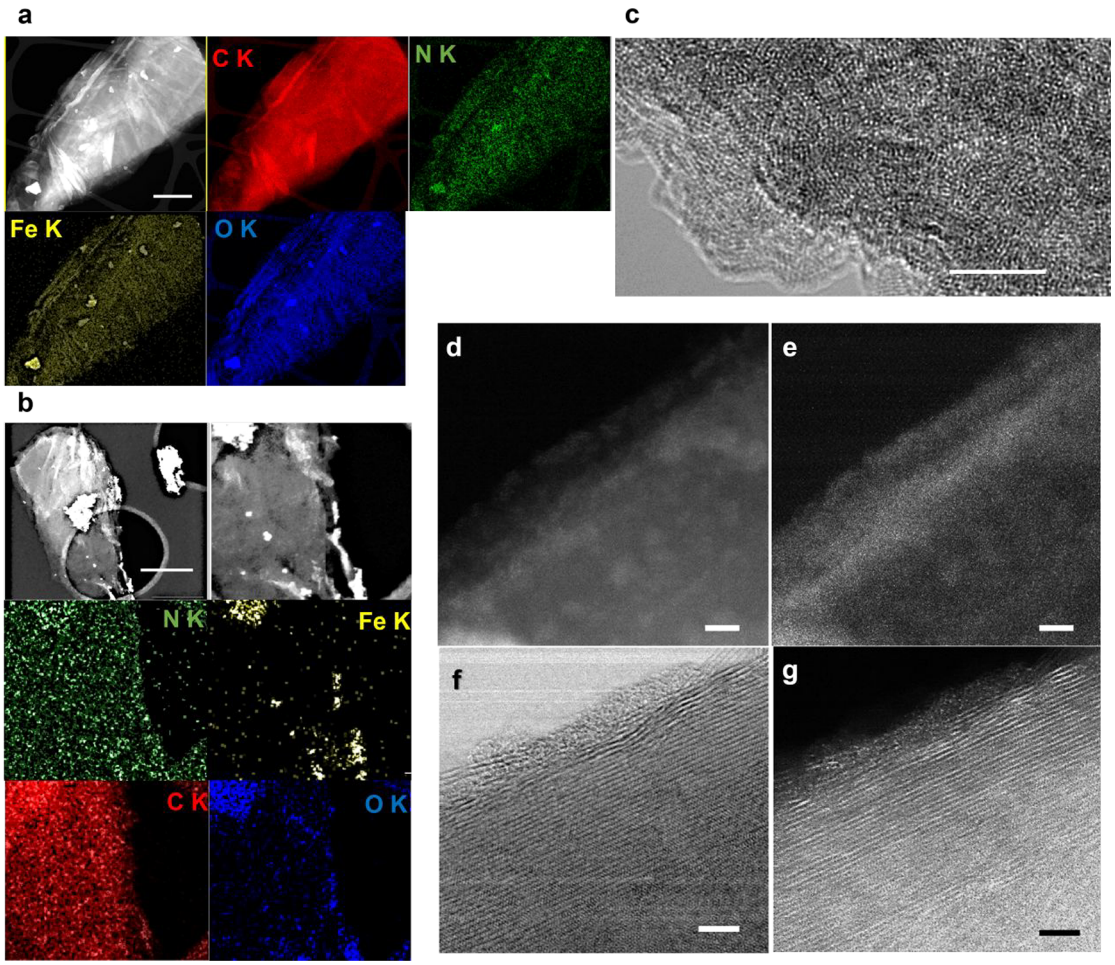

Figure 3. Multilength-scale electron microscopy characterization of the as-prepared electrocatalysts. (a) Low-magnification HAADF-STEM image and corresponding elemental mapping images of FeOOH/OC. Scale bar is 1 μm. (b) Low-magnification HAADF-STEM image and corresponding elemental mapping images of FeOOH/NC. Scale bar is 200 nm. (c) HRTEM image of the large particle in FeOOH/NC. Scale bar is 5 nm. (d) HR HAADF-STEM image of FeOOH/NC. Scale bar is 5 nm. This image, adapted from ref 41, is licensed under CC BY 4.0. (e) The corresponding SE-STEM image. This image, adapted from ref 41, is licensed under CC BY 4.0. (f) BF-STEM image of FeOOH/NC. Scale bar is 3 nm. (g) Corresponding HAADF-STEM image.

morphology and sparsely cover the support surface. The secondary electron (SE)-STEM image (Figure 3e) provides a clear visualization of the surface topology of this sample, showing the thin-film nature of these nanostructures.

In Figure 3f and g, the thickness of the disordered thin film is less than 3 nm. The images also show that the edges of the graphene layers terminate into the FeOOH film, which is a prerequisite for a stronger interaction between the support and the FeOOH nanostructures as well as for electron transport through this interphase. This is a characteristic of the low-nuclearity species on these samples (for an example, see also Supplementary Figure S10e).

These thin-film patches coexist with larger NPs, and no large difference in the relative distribution of the species was clarified by electron microscopy for differently functionalized supports. However, the comparative surface electronic structure analysis of the Fe species for the differently functionalized supports by XPS and NEXAFS under UHV conditions allowed use to identify a few reduced Fe(II) states on the N-functionalized support already in the freshly prepared samples, demonstrating different metal−support interfacial interactions for the two systems (Supplementary Figure S11). Due to the different probing depth of these techniques, it is possible to infer that these sites are localized on low-dimensional ferrihydrite nanostructures and that they are generated by the chemical interaction with surface nitrogen atoms on the graphitic support, as expected based on a previous computational study.[6]

Electrocatalytic Performances. The results of the electrocatalyst performances obtained using the GPEC as well as the *in situ* electrochemical cell (ISEC) are presented; the former for the electrocatalytic tests at atmospheric pressure and the latter at pressures in the millibar range. The results of the gas-phase carbon dioxide reduction over FeOOH/OC and FeOOH/NC using the GPEC are reported in Figure 4a. These data refer to an average value determined after 1 h tests at two applied potentials, namely −1 and −1.5 V vs Ag/AgCl. The results of the carbon dioxide electroreduction are reported in terms of carbon dioxide reduction products formed in micromoles per hour (μm/h). Specifically, C_1 (methanol), C_2 (acetaldehyde), and C_3 (acetone and isopropanol) products were observed. Only traces of ethanol were detected, while no CO or other organic products were observed. Methanol and isopropanol are the two main products detected at −1 V vs Ag/AgCl. At this potential, the total productivity in the CO_2 reduction is about 8.4× higher for FeOOH/NC than FeOOH/

https://doi.org/10.1021/acscatal.1c04296
ACS Catal. 2022, 12, 411−430

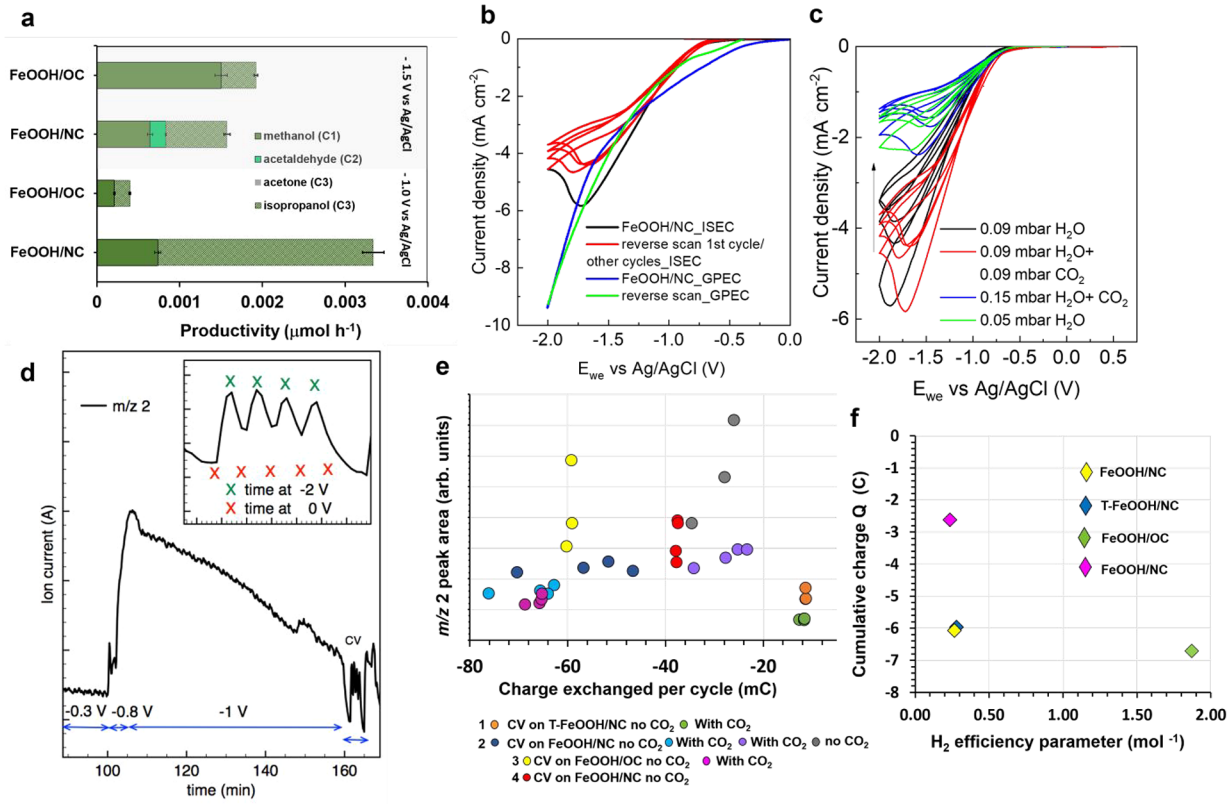

Figure 4. Gas-phase electrocatalytic tests using the GPEC and ISEC. (a) Average productivity (mmol/h) toward carbon dioxide reduction products as indicated in the legend for FeOOH/NC and FeOOH/OC during 1 h of CO_2 reduction in the gas-phase electrocatalytic cell (GPEC) at 1 bar. Tests were carried out at −1 and −1.5 V vs Ag/AgCl. The electrolyte solution at the CE side was 0.5 M $KHCO_3$. The error bar refers to the average error observed of 5%. (b) Cyclic voltammograms under 1 bar of CO_2 atmosphere for FeOOH/NC for the GPEC (blue and green) and under 0.09 mbar of H_2O and 0.09 mbar of CO_2 for the ISEC (red and black). (c) Cyclic voltammograms obtained for FeOOH/NC under different gas atmospheres, as indicated, using the *in situ* electrochemical cell. The voltage sweep rate is 50 mV/s in both GPEC and ISEC experiments. (d) Evolution of m/z 2 in the mass spectrum during the *in situ* characterization of FeOOH/NC, with the inset showing the detail of the oscillation during the CV. Spectroscopic data relative to this mass spectrum are reported in Figures S16b, 17b, and 18b. The CV region corresponds to the data in panel e (purple circle), and the CA region corresponds to the data in panel f (magenta rhombus). (e) m/z 2 peak area vs charge exchanged during each voltammetric cycle for selected *in situ* experiments (1−4 in the legend) in the presence and absence of carbon dioxide. Each row of the legend corresponds to an *in situ* experiment over a sample as indicated, whereas the sequence corresponds to the order in which the experimental conditions were investigated. The color code indicates several cycles run consecutively under the same conditions, with the current decreasing with the number of cycles. (f) Cumulative charge exchanged during CA *in situ* experiments at −1 V vs Ag/AgCl vs the H_2 efficiency parameter for various electrocatalysts as indicated. These data correspond to the spectroscopic measurements reported in Figures 5 (yellow rhombus), 6 (blue rhombus), and S16a, S17a, and S18a (green rhombus).

OC, indicating the beneficial effect of N-doping the carbon substrate.

The side formation of H_2 was also observed (Supplementary Table S2 and S3), which was derived largely from the GDL support. Supplementary Tables S2 and S3 report the product productivities at various voltages from −0.5 to −1.5 V vs Ag/AgCl for FeOOH/NC and FeOOH/OC, respectively.

The total productivity becomes noticably lower at the more negative potential for FeOOH/NC due to both the enhanced H_2 formation limiting protons and electrons for the selective reduction of CO_2 and electrocatalyst deactivation. For FeOOH/OC, the highest productivity of carbon dioxide reduction products occurs at a lower cathodic potential; however, the formation of H_2 was higher at these conditions, and some deactivation was noted (Supplementary Table S3).

We also note that at −1 V vs Ag/AgCl the catalysts remained stable for at least 20 h of time-on-stream, while at a more negative voltage (−1.5 V vs Ag/AgCl) the deterioration of the performance with time-on-stream was detected. Nevertheless, the good stability observed over this time period indicates that the samples are suitable for mechanistic studies at potentials down to −1 V vs Ag/AgCl. This potential and above were chosen for the mechanistic study.

In terms of the carbon Faradaic efficiency, which was calculated considering that methanol formation is a $6e^-$ reduction while isopropanol formation is an $18e^-$ reduction, the carbon Faradaic efficiency to isopropanol at −1 V vs Ag/AgCl passeed from about 73% to over 91% when going from FeOOH/OC to FeOOH/NC. Note that while these high values refer to the Faradaic efficiency to the carbon product, H_2 also forms, lowering the total selectivity (see Supplementary Table S2 and S3).

Isotopic labeling experiments with $^{13}CO_2$ and $KH^{13}CO_3$ over FeOOH/NC at −1 V vs Ag/AgCl were performed to track the source of C in the products observed. The MS spectra relative to the GC peaks associated with methanol and isopropanol are shown in Supplementary Figures S12 and S13 and show patterns diagnostic of ^{13}C methanol ($^{13}CH_3OH$, m/z = 33) and ^{13}C isopropanol ($^{13}CH_3-^{13}CHOH-^{13}CH_3$, m/z = 47), respectively. For comparison, the MS spectra obtained

https://doi.org/10.1021/acscatal.1c04296
ACS Catal. 2022, 12, 411−430

from the same test but feeding a natural abundance of CO_2 and using aqueous 0.5 M $KHCO_3$ as the analyte is also reported in Supplementary Figures S12 and S13.

These experiments allowed us to rule out that the products detected during the CO_2 electrocatalytic reduction were derived from the carbon substrate itself, which is consistent with our blank and control experiments[60] on carbon-supported systems in inert gas and other literature studies.[61]

Indeed, activity and selectivity trends are consistent with previous indications[29] that N-doping promotes the activity and the selectivity of Fe-oxide species supported on carbon to isopropanol in the carbon dioxide gas-phase electroreduction. This result is important for this study considering that the systems investigated here were prepared using a different procedure and a different carbon support than those in the previous work, where Fe−N−C systems were screened for this reaction.[29]

Here, our aim was to minimize any additional sources of carbon that would add complexity to the spectroscopic analysis of the species in the electrical double layer. Therefore, we did not use the thin film method for the electrode preparation, which would require the preparation of a catalyst ink using an organic binder, normally a Nafion solution. Moreover, constraints dictated by the assembly of the electrode in the *in situ* cell led us to design a self-standing electrode by directly impregnating the graphitic carbon paper gas diffusion layer with the metal active phase. This carbon paper is highly graphitic as seen in Figure 3d−g, whereas the carbon nanotubes (CNTs) used in the previous study for the gas-phase electrocatalytic conversion of CO_2[29] presented a thick surface layer of highly disordered pyrolytic carbon.[29]

The Fe speciation was also different in the previous study.[29] Big particles of magnetite encapsulated inside the channels of the nanotubes were found together with highly abundant dispersed FeOOH clusters on the external surface of the nanotubes. Here we find Fe(III)−OOH species of a different nuclearity.

The corresponding trends between the previous study[29] and this current one allow us to narrow down the identification of the electroactive species to highly dispersed or quasi-2D nanostructures on the carbon support, such as Fe-OOH nanoclusters, and ferrihydrite-like thin layers interacting with the N-functionalized edges of the support, as exemplified in Figure 3.

We also note that, with respect to the previous study on chemically identical FeOOH/NC for the liquid phase CO_2RR,[6] here the preparation and CO_2 reaction conditions are optimized to enhance the formation of isopropanol, which occurs at a lower applied potential (more cathodic) than the formation of acetic acid observed for the same system in the $KHCO_3$ electrolyte. Yet, the beneficial effect for C−C coupling exerted by N-functionalization was also observed, thereby corroborating the fundamental interplay between the nuclearity of the FeOOH species and their interaction with the support to realize efficient electron transfer at the support−FeOOH−CO_2 interphases. We postulate that in both the liquid phase and gas-phase approaches the low-dimensional CO_2-bearing nanostructures are the electroactive species; however, these species should undergo different structural dynamics triggered by the potential and the nature of the interphase, leading to a reaction mechanism for the reduction of the chemisorbed species that is different between the two approaches. In the gas phase, intuitively the limited availability of H^+ should favor heavier products.

In Figure 4b, we compare the cyclic voltammetry (CV) tests for FeOOH/NC realized under the CO_2 atmosphere using the GPEC and ISEC. With the GPEC, we observed a monotonic increase in the current density and identified two onset potentials for reduction. The first one is at approximately −0.5 V vs Ag/AgCl, whereas the main faradaic process is at −1.75 V vs Ag/AgCl. With the ISEC, we see a redox wave showing a maximum value and a subsequent decrease of the current density, which is typical of an electron transfer process limited by diffusion.

This difference appears to be a consequence of the lower-pressure condition and the low wetting realized in the APXPS experiments as compared to those in the GPEC and thus the different interfacial electrocatalyst and gas-phase compositions realized in the two cells. To explore the extent of the redox chemistry involving CO_2 during the *in situ* APXPS and NEXAFS studies, we compared the CV obtained in the ISEC cell in a water-only atmosphere with the CV recorded in the same cell after CO_2 was added to the chamber (Figure 4c). The CV measured in the APXPS chamber under 0.09 mbar of H_2O shows a broad redox wave with an onset at about −0.8 V vs Ag/AgCl and a maximum at about −1.95 V. This redox wave becomes narrow and the maximum shifts toward a higher voltage (about −1.75 V) when CO_2 (in a ratio of about 1:1 with respect to H_2O) is cofed into the XPS chamber, revealing a diffusion-controlled electron transfer below −1.75 V. During consecutive cycles, the total charge exchanged decreases following the decrease of the water partial pressure. As the total charge exchanged continues to decrease, the maximum of the reduction wave slightly shifts to higher potentials (about −1.5 V). The presence of the CO_2 cofeed contrasts the decay of the maximum wave with the number of cycles, but the effect is still present. The observed decay of the performance is due to diffusion-limited electron transfer.[62]

These CV data indicate that, in the conditions realized in the APXPS measurement chamber, the faradaic processes are dominated by the water chemistry, as probed by a clear response of the H_2 signal (m/z 2) in the QMS spectrum (Figure 4d) while sweeping the voltage during the CV. Indeed, we expected these results considering side H_2 formation.

Yet, the presence of CO_2 influences the redox cathodic process, confirming CO_2 redox chemistry. Specifically, the CV curve is mainly composed of the steep faradaic process of the HER (hydrogen evolution reaction) with an onset potential at approximately −0.75 V, whereas the CO_2RR appears to be partially overlapped with the HER but shifts to potentials higher than the HER (lower overpotential) as the latter becomes more limited by diffusion.

For a quantitative analysis, we compare the peak area of the fragment m/z 2 generated in the mass spectrum as a consequence of the transient evolution of H_2 during the potential sweep in a CV cycle (Figure 4d) to the charge transferred during the cycle, which was obtained by integrating the corresponding peak area in the current versus time plot of the same cycle. Figure 4e summarizes the data obtained for several *in situ* experiments as indicated in the legend (experiments 1−4). We note that the *in situ* performances of chemically identical electrocatalysts might differ in absolute value (see experiments 2 and 4) due to the different conditions realized by the water transport through the membrane and the pumping condition in the evacuated chamber. However,

https://doi.org/10.1021/acscatal.1c04296
ACS Catal. 2022, 12, 411−430

regardless of the nature of the samples, the current exchanged either increases or remains the same after the addition of carbon dioxide, but the amount of H_2 evolved decreases, indirectly confirming the formation of some CO_2 reduction products. We can also see that under a carbon dioxide-free atmosphere, FeOOH/OC (experiment 3) shows a higher level of H_2 formation than FeOOH/NC (experiment 2). The addition of CO_2 in the XPS chamber initially leads to a higher current for FeOOH/NC, while the H_2 formation is similar for both electrocatalysts. This observation confirms the higher selectivity of FeOOH/NC toward carbon dioxide reduction products, although later the charge transferred versus H_2 formed seems comparable for the two systems. Also, these results are consistent with the higher H_2 formation observed for FeOOH/OC in the GPEC (Supplementary Table S3). We observed that the electrocatalyst performance deteriorates with time, as seen in the significant increase in the amount of H_2 formed for FeOOH/NC with time even under a carbon dioxide atmosphere (sequence in experiment 3).

Therefore, it is correct to infer that there is a competition between the HER and the CO_2RR reactions. As a consequence, the selectivity will depend on the ratio of the reaction rates. From Figure 4c, it appears evident that the CO_2 reduction occurs at a slightly higher potential than the HER and, therefore, operations at a higher applied potential are important for maximizing the CO_2RR versus the HER. Likewise, maintaining a low water pressure is also important to limit the HER versus the CO_2RR. We note that the water partial pressure in the XPS chamber detected by QMS is higher than the CO_2 partial pressure for FeOOH/OC, whereas the opposite is true for the more CO_2RR-active FeOOH/NC and T-FeOOH/NC (Supplementary Figure S14a). We believe that this pressure difference is naturally generated by the different hydrophobic and hydrophilic properties of the functionalized carbon support and could explain the relatively higher observed selectivity toward C_{2+} products (Figure 4a) for the FeOOH/NC. This explanation shows that many factors can be used to tune the activity and selectivity for this reaction. Control of the relative concentration of H_2O and CO_2 on the surface is also an important aspect to consider when analyzing the mechanism of C_3 formation during the CO_2RR. Hence, these *in situ* ISEC experiments can provide unique indications concerning the mechanism of CO_2 reduction products.

To establish a robust structure−function correlation, it is imperative to characterize the performances of the samples using the *in situ* cell. To this end, we also attempted a quantitative analysis of the catalytic performances of the electrocatalysts during the spectroscopic measurements under potentiostatic control. In this case, the H_2 evolution gave rise to a sharp increase of the m/z 2 signal following the application of the potential, with consequent rapid decay as the cell was allowed to equilibrate at the open circuit potential (OCP) (Figure 4d). Also, in this case we use an indirect comparative analysis based on the quantification of the amount of H_2 evolved. The detection of other mass fragments related to CO_2 reduction products was very challenging due to the very low amounts formed, although in some cases the evolution of m/z 45 was observed upon polarization at −1 V (Supplementary Figure S14b-d).

Figure 4f summarizes the results of several experiments by reporting the cumulative charge exchanged at −1 V vs Ag/AgCl under a continuous feed of carbon dioxide as a function of the H_2 efficiency parameter, representing the ratio of the amount of H_2 formed to the current measured. Thus, a higher value indicates a higher H_2 efficiency and vice versa. This comparative analysis shows that given similar charge transferred, FeOOH/OC shows a much higher H_2 efficiency than FeOOH/NC, consistent with GPEC results (Table S2 and S3). As a consequence, FeOOH/NC will be more productive toward carbon dioxide reduction products. We also see that given a similar H_2 efficiency parameter, FeOOH/NC is less selective toward carbon dioxide reduction products in one of the experiments (magenta rhombus versus yellow rhombus),- which is probably a consequence of the reactive atmosphere. However, general trends in performances were confirmed and consistent between GPEC and ISEC; these results provide direct evidence of the importance of the structure of the electrochemical interface, which is determined not only by the nanostructural characteristic of the electrode but also by long-range and short-range dispersive interactions and mesoscale phenomena that control the availability of the reagents (water and carbon dioxide) at the interphase.

***In Situ* Surface-Sensitive APXPS Study.** We focus here on the interfacial structural dynamics observed for FeOOH/NC upon constant polarization under a humidified CO_2 atmosphere to provide insight into the origin of the high selectivity toward isopropanol among the carbon dioxide reduction products. The surface sensitivity of APXPS enables us to increase the sensitivity of the measurement toward the electrically active interface.

The gas environment in the APXPS chamber during the experiments was composed of a constant CO_2 flow (0.09−0.1 mbar) that was fed via a mass flow controller and a variable H_2O pressure (0.05−0.09 mbar). The variable H_2O pressure in the chamber results from the transport of the aqueous electrolyte solution (H_2SO_4 0.05 M) through the polymeric electrolyte membrane into the measurement chamber.

For our *in situ* spectroscopic studies, we chose two potentials, one in the region dominated by capacitive processes (−0.3 V vs Ag/AgCl) and the other one at the condition where the productivity for CO_2 reduction products was found to be the highest in the bench-scale tests (−1 V vs Ag/AgCl). In this way, the changes of the surface species due to CO_2 reduction can be assessed. The XPS spectra were fitted using the model described in the Experimental section derived from the annealing experiments presented in Supplementary Figures S1−S4 of the Supporting Information and is discussed in detail therein. The peak assignments of the spectral components derived from the fits of the C 1s, Fe $2p_{3/2}$, and O 1s regions are given in Tables 1−3 in the Experimental section, respectively. The annealing experiment was also important to identify structural transformations involving the formation of the Fe−C species described below and found at a BE of 283.6 eV,[63−65] which as it turns out are exclusively formed due to the interaction of the surface Fe phase with CO_2 under polarization during the *in situ* electrocatalytic measurements. Indeed, as it is shown in Supplementary Figure S1, this species was not formed during the annealing experiment, ruling out its formation as a consequence of the interaction of the Fe phase with the carbon support.

The C 1s XPS spectra for FeOOH/NC at −0.3 and −1 V vs Ag/AgCl in Figure 5a and b, respectively, are recorded during the experiment reported in Figure 4f (yellow rhombus) at different kinetic energies of the photoelectrons (KE) to afford a compositional profile at different depths across the reactive interface. In this *in situ* experiment, this sample showed a

https://doi.org/10.1021/acscatal.1c04296
ACS Catal. 2022, 12, 411−430

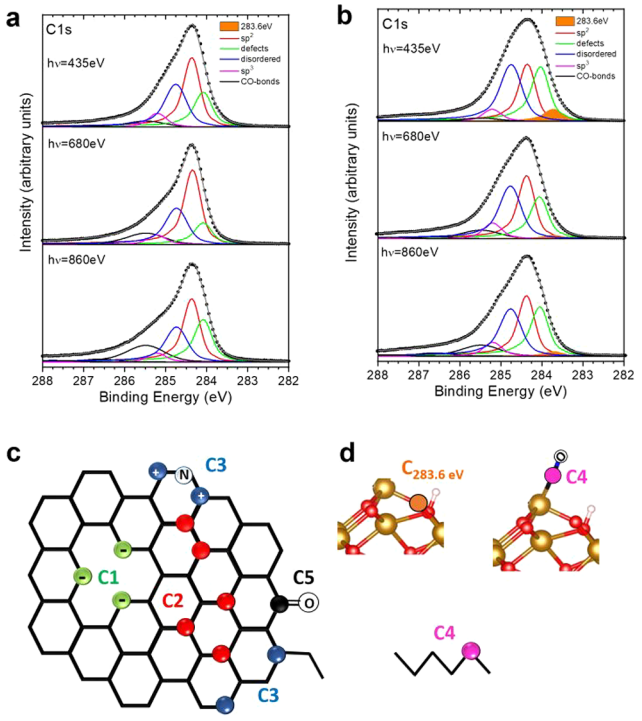

Figure 5. Dynamics of C species during electrocatalytic conversion of carbon dioxide in potentiostatic conditions. (a) Fitted C 1s spectra measured for the FeOOH/NC electrocatalysts at different excitation energies as indicated under 0.09 mbar of CO_2 and 0.09 mbar of water at a −0.3 V vs Ag/AgCl (measured cathodic current around −0.7 mA). (b) Spectra at −1 V vs Ag/AgCl (measured cathodic current ranging from −1.3 to 1.4 mA) during the experiment reported in Figure 4f (yellow rhombus). (c) Chemical configurations of the carbon species on the support and corresponding color-coded peak notation in the fitted C 1s XPS spectra. (d) CO_2-related chemisorbed carbon species on the Fe phase and corresponding color-coded peak notation in the fitted C 1s XPS spectra. The support color scheme for O, Fe, and H in the ferrihydrite slab is red, dark yellow, and white, respectively.

relatively higher CO_2 reduction efficiency. Using the fitting procedure summarized in Table 1,[44,48] we consider that the C−O bond species (C5 component, black line) are due to π-system electron-withdrawing oxygen functionalities of the substrate, which are more clearly visible at higher depth, as well as the chemisorption of CO_2-related species on the Fe phase. The components describing the electronic structure of C atoms with localized charge accumulation surrounding in-plane point defects in the graphene layers (C1, green line) and sp^2 carbon in graphite (C2, red line) are related to the graphitic support. The C3 component (blue line) was associated with disordered graphite and accounted for sp^2/sp^3 moieties and either dangling bonds at the periphery of the graphene layers or large holes in the graphitic structure. From an electronic structure viewpoint, this component can account for any form of C atoms at the periphery of the graphene layers that are characterized by some extent of localized charge depletion due to the neighboring atoms,[48,64] including the N edge-sites.[42,43] Indeed, this component is formed on CNTs upon N-functionalization by a thermal treatment in NH_3 at elevated temperatures,[42,43,45] which is known to not only introduce N species but also to exert an etching effect on the graphite structure, generating more edge sites. This species is consistently found here more abundantly on FeOOH/NC (Supplementary Figure S11c).

The component related to the sp^3 carbon (C4, magenta line) can be due to either an amorphous carbon component of the support or chemisorbed reduced species related to either the electrolyte or CO_2 on the electrocatalytic surface. A support scheme in Figure 5c shows the assignment of the XPS peaks to the various chemical configurations of C on the support, whereas Figure 5d describes the assignment of the various C species chemisorbed on the Fe phase.

Noteworthy, at −0.3 V vs Ag/AgCl the amount of C−O species described by the C_5 component increases from the surface toward the bulk at both potentials, suggesting that this component is due mainly to the functionalized C support buried underneath the Fe−OOH nanostructures and in a minimal part to the C−O species formed as a consequence of the CO_2 chemisorption at the surface. On the contrary, the amount pure sp^3 carbon or C−O and C−H chemisorbed on the Fe component (C4, magenta line) decreases slightly from the surface toward the bulk as expected for chemisorbed species. The amount of the C3 component (blue line), due to peripheral atoms of small graphite flakes with a high edge to basal plane ratio, decreases from the surface toward the bulk.

At the lower voltage (−1 V vs Ag/AgCl) at which carbon dioxide is reduced, the transformations involve a decrease of the amount of C−O components and an increase of amount of the peripheral sp^3/sp^2 dangling bonds of the support (C3 component) as well as the appearance of a new component at 283.6 eV (orange peak in Figure 5b), which occurs most abundantly in the topmost layer ($h\nu$ = 435 eV). A carbon component at 283.6 eV was found forming over Fe, Ni, and Fe−Ta catalysts during the catalytical chemical vapor deposition of monolayer graphene[64] and CNTs[65] and was attributed to weakly bound atomic C dissolved in the metal phase; this should be distinguished from atomic C on the metal surface, which would appear at even lower BEs.[64] A component at a similar BE was also found in the amorphous $Fe_{1-x}C_x$ films.[63]

We also note that at the excitation energy of 435 eV, the C−O bond component is almost suppressed at −1 V vs Ag/AgCl, which suggests that the part of the chemisorbed CO species contributing to the C5 component were quantitatively converted at this potential into reduced C species.

We consider the nonlinear trends observed in the distribution of some of the C species of the support (C1 and C2) with an increased probing depth at the two different voltages as an expression of an inhomogeneous and dynamic interface under polarization. This interface is structurally inhomogeneous in terms of the exposed C-support surface and immobilized Fe−OOH nanostructures interacting with the edge termination of the graphitic layers or being deposited on the basal plane of graphite support, with either a weak interaction for larger particles or a stronger interaction for low nuclearity species at the edge of the graphene layers. These nanostructures will contribute differently to the XPS spectra at the different probing depths.

Supplementary Figure S15 of the Supporting Information aims to clarify the volume probed by XPS at different excitation energies across the C support−Fe phase interface visualized by TEM. Briefly, we can consider that the bare support surface and the surface of the Fe phase will be probed by the most surface-sensitive measurements (for a perfectly planar nonporous surface, the probing depth for C 1s at $h\nu$ =

https://doi.org/10.1021/acscatal.1c04296
ACS Catal. 2022, 12, 411−430

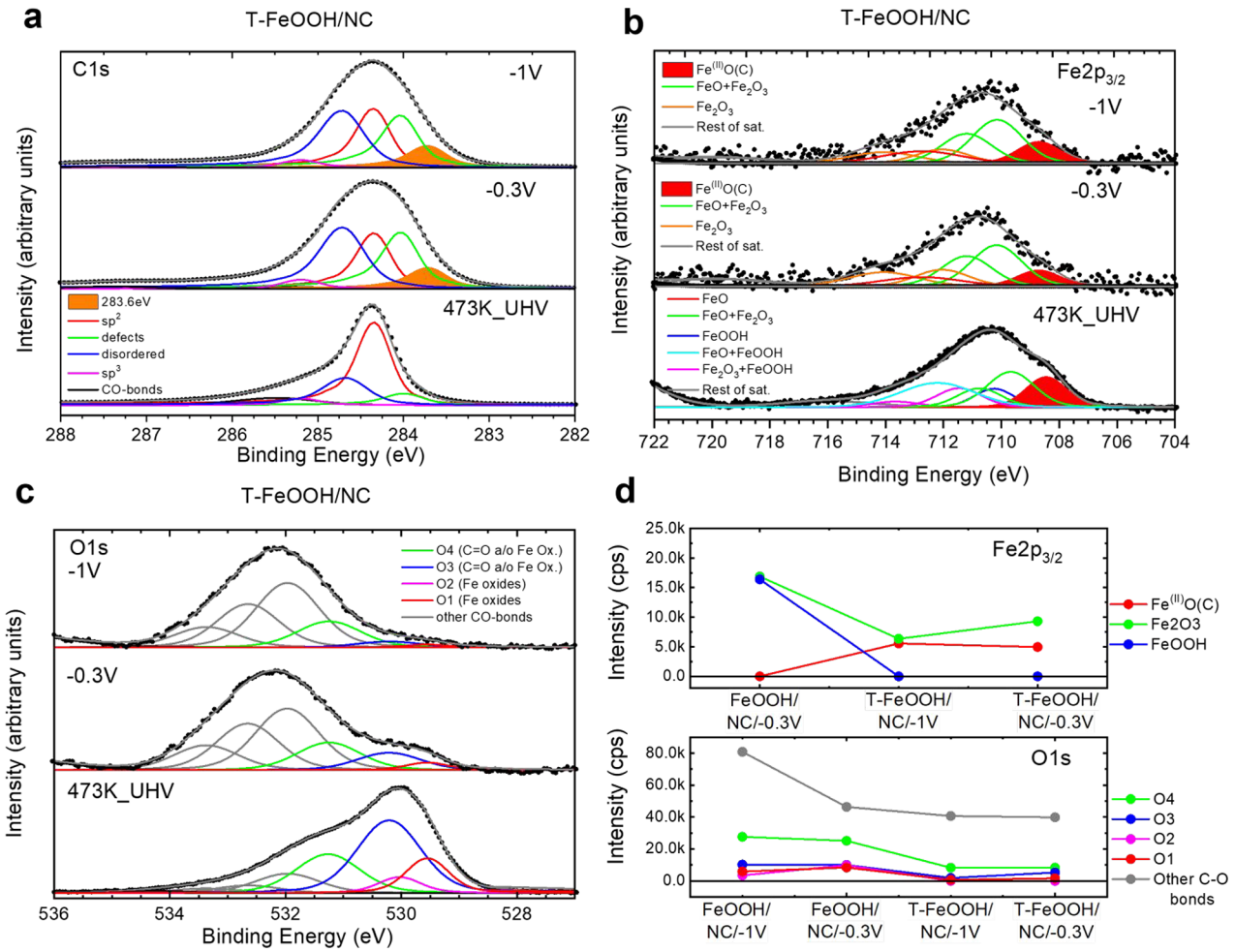

Figure 6. Influence of electrode reduction on the dynamics during the electrocatalytic conversion of carbon dioxide in potentiostatic conditions. (a) Fitted C 1s XPS spectra, (b) fitted Fe 2p XPS spectra, and (c) fitted O 1s XPS spectra measured during the *in situ* experiments of a thermally treated FeOOH/NC electrode (T-FeOOH/NC) at different conditions as indicated. The spectra at −0.3 and −1 V vs Ag/AgCl were measured at KE = 150 eV. At −0.3 V vs Ag/AgCl, the measured cathodic current was around −3 μA at 0.15 mbar of total pressur,e whereas at −1 V vs Ag/AgCl the measured cathodic current ranged from −1.6 to −1 mA at a total pressure of 0.15 mbar. The catalytic performances during this experiment are reported in Figure 4f (blue rhombus). (d) Relative intensity of Fe and O species during this experiment.

435 eV is ca. 0.5−1.8 nm),[66] and the Fe−C−substrate interface for the thin Fe oxyhydroxide films will be probed at a higher depth (for a perfectly planar nonporous surface, the probing depth for C 1s at $h\nu$ = 860 eV is ca. 1.2−3.6 nm).[66] The abundance of single Fe atoms should decrease at higher depths. These inhomogeneities and dynamics are particularly evident by the fact that the components due to the graphitic support, namely the graphitic C component (red line) and the point defect component (green), change across the interface and at the different potentials.

Although there is not a unique explanation for this, we believe that in the most surface-sensitive spectrum, the graphitic component (red component) and the defective component (green component) are due to the bare ordered support, while the C3 component accounts for the edges of the graphene layers (disordered graphite component) either exposed or decorated with single Fe atoms and 2D FeOOH clusters. The edge termination of the graphite layers underneath the Fe oxyhydroxide thin film in Figure 3 will be probed at a higher excitation energy (Supplementary Figure S15). The fact that the edge sides of the disordered graphite components (blue line) as well as the defective component (green line) exhibit higher intensities across the probed volume at a lower voltage while the graphitic component has a lower intensity compared to the spectra at a higher voltage indicates that these low-nuclearity and low-dimensional Fe species interacting with the edge planes of the graphitic support undergo structural transformations under cathodic polarization. This is consistent with either the generation or the exposure of buried edge terminations interacting with the Fe phases and at the same time generating or exposing point defects on the basal planes. The sintering of large particles on the basal planes of the graphitic structure could also explain the decrease of the amount of the graphitic component.

Previously we identified *in situ* formed Fe(II) species as active sites for CO_2 reduction.[6] To identify the surface structural dynamics of Fe(II)-abundant electrocatalysts, we have reduced FeOOH/NC at 473 K (T-FeOOH/NC). This reduction was monitored by *in situ* NEXAFS at the Fe L-edges[41] in combination with electron diffraction to confirm that the ferrihydrite-like phase was partially reduced, leading to a segregated phase of FeO in Fe_3O_4.[41]

In Figure 6 we report the *in situ* XPS characterization of this reduced sample during the CO_2RR at different voltages

https://doi.org/10.1021/acscatal.1c04296
ACS Catal. 2022, 12, 411−430

together with the relative abundance of the species. This experiment is related to the catalytic data reported in Figure 4f (blue rhombus) that show relatively low H_2 production and thus a higher CO_2 reduction product selectivity, which is comparable to that of the previous samples.

In Figure 6a, the C 1s XPS core levels measured at −0.3 and −1 V vs Ag/AgCl are reported together with the spectrum of the sample annealed at 473 K in UHV. While the reduction of Fe(III) to Fe(II) was confirmed during the thermal pretreatment, one must bear in mind that the annealed sample was then briefly exposed to air before being mounted onto the ISEC for the *in situ* EC study. As a consequence, the Fe(II) surface species are partly reoxidized and hydrated Fe(III) species.

In this annealed sample, we can see that the abundance of the Fe−C component (orange line) slightly increases as well as the abundance of the graphite peripheral C species (C3 component, blue line). As reported in dedicated literature, the dissolution of C atoms in Fe oxides also leads to an Fe−C component at the same BE as that for FeO[64] (both contributing to the red component in Figure 6b). We should point out that there is a more pronounced change in the C speciation for the *in situ* measurements at −0.3 V vs Ag/AgCl when compared to the UHV measurements, which indicates that most of the structural transformation occurred during the preceding CV under CO_2. Nevertheless, during these spectroscopic measurements the performance of the electrocatalyst was shown to be selective toward CO_2 reduction; therefore, these dynamics can be correlated to the active surface. We analyzed the O 1s core level in Figure 6c by considering components related to FeOOH and FeO phases (in red, magenta, blue, and green) and, for the polarized samples, those related to the C−O species within the electrical double layer. The latter were found in a broad range of BEs, also overlapping with Fe−O species. C═O species contributing to the green and blue components are those chemisorbed on the Fe phase, whereas the gray components are related to C−O species on the support or electrophilic or acidic CO_2-derived chemisorbed species. We can see that the amount of Fe(III)−O species (O1 and O2 components) decreases as the potential decreases whereas Fe(II)−O are still well pronounced (O3 and O4 components). This observation suggests the almost quantitative reduction of the FeOOH phase, which is consistent with the changes observed in the Fe 2p XPS spectrum (Figure 6b) when accounting for the disappearance of the FeOOH related components and the increased abundance of the lower BE Fe(II) species accompanied by a shift of the satellites to lower BEs.

These dynamics can be better evaluated by analyzing the peak intensities of the O 1s and Fe 2p components at the different experimental conditions, which are reported in Figure 6d for both FeOOH/NC and T-FeOOH/NC samples. For T-FeOOH/NC, we note a small increase of the abundance of Fe(II) at the lowest voltage (−1 V), probably due to an oxide phase with dissolved interstitial C atoms Fe(II)−O(C). This observation is supported by a similar increase in the amount of the Fe-dissolved atomic or weakly bound atomic C peak in the C 1s region (orange peak). We also note a small increase of the amount of C−O related components, which may be related to the CO chemisorbed species (O5−O7 components). In contrast, FeOOH/NC is a mixture of solely Fe(III) oxides, where the absolute abundance of Fe species appears to be much higher than that for T-FeOOH/NC. Noteably, we can see that the amount of CO species (O5−O7) increases in a more pronounced manner when the potential for FeOOH/NC is lower. We consider this as a result of the higher Fe abundance for this sample in which a higher population of CO_2 chemisorbed species can be accommodated. However, given that a cathodic polarization is applied, it is possible to infer that these acidic species are not located in regions where faradaic cathodic processes take place (e.g., few-layer Ferrihydrite) but instead on the surface of poorly conductive larger particles, contributing to most of the signal in both the Fe 2p and O 1s XPS spectra for this sample. Note that for both samples, FeOOH/NC and T-FeOOH/NC, the changes of the Fe oxidation state due to the polarization are very small. Both samples show similar performances (blue and yellow rhombus in Figure 4f).

In addition, the N 1s region was monitored for each sample under *in situ* conditions to account for possible changes of the N of the substrate (not shown). Under the surface-sensitive condition applied, here no changes were observed. The evolution of both the Fe states and the N states will be discussed further in the next section.

Near-Surface Sensitive *In Situ* NEXAFS Study. FeOOH/NC and FeOOH/OC *in situ* dynamics were also analyzed by means of NEXAFS spectroscopy in terms of both the total electron yield (TEY) and the Auger electron yield (AEY). These experiments put in evidence how ferrihydrite transforms by a reaction with CO_2 under the conditions realized in the *in situ* chamber. Fe L_3-edge NEXAFS spectra of FeOOH/OC and FeOOH/NC are shown in Supplementary Figures S16a and S16b, respectively.

The spectra were recorded in UHV conditions and in the *in situ* electrochemical cell at −0.3 V vs Ag/AgCl. As mentioned before, this potential enables us to characterize the adsorbates present before the electrocatalytic turnover takes place. The spectra of both samples, FeOOH/NC and FeOOH/OC, in UHV are characterized by the resonances R1 (2p → 3t2g) at 709 eV and R2 (2p → 3eg) at 710.4 eV, which are typical of Fe(III) species. The difference spectrum of these samples shows a more intense resonance at a low excitation energy for the FeOOH/NC, which is a signature of a few Fe(II) sites (Supplementary Figure S11a).[41] Besides Fe(III) species in octahedral sites, the ferrihydrite-like structure also presents Fe(III) species in tetrahedral sites, which were identified in the Fe L-edge NEXAFS spectrum as an additional resonance between the main t2g and eg resonances of the Fe(III) in O_h symmetry.[67]

Interestingly, for FeOOH/OC we observed a loss in the signal of only the latter peak, which represents the tetrahedral sites, under polarization at −0.3 V vs Ag/AgCl. This signal loss could be the result of either the chemisorption of both CO_2 and H_2O on undercoordinated tetrahedral sites or a structural transformation due to the polarization. In contrast for the FeOOH/NC sample, not only did the tetrahedral sites disappear but the Fe(II) species present in small amounts also decreased, as can be seen from the reduced intensity of the lower energy resonance. This diminution is likely related to the coordination of CO_2, leading to a higher degree of *in situ* transformation. Note that at a more negative potential (−1 V vs Ag/AgCl), no further significant changes in the Fe L-edge NEXAFS spectrum (not shown here) could be seen.

From these observations, we conclude that only a small fraction of the sample is exposed to the reactive atmosphere while most of the Fe species remain unchanged, which is

https://doi.org/10.1021/acscatal.1c04296
ACS Catal. 2022, 12, 411−430

consistent with a picture in which the Fe L-edge NEXAFS signal is dominated by the contribution from large particles.

Moreover, the observation that large parts of the sample are unaffected by the polarization even at −1 V vs Ag/AgCl can be explained by accounting for the poor electron conductivity of the large ferrihydrite-like particles. The resistivity of goethite (α-FeOOH) and lepidocrocite (γ-FeOOH) thin layers is around 1×10^9 Ω cm compared to those of the equivalent oxide layers, which range from 2.4×10^6 to 1.1×10^8 Ω cm.[68] Although it is not possible to directly measure the electronic conductivity of our ferrihydrite-like thin layers with respect to larger particles, the resistivity values reported above indicate that for particles larger than a few nanometers the resistivity is too high to allow an efficient transport of electrons to the surface of large ferrihydrite particles (20−50 nm), even via the application of a potential. This is in agreement with the use of iron oxide- or hydroxide-based electrode materials for supercapacitors.[69]

Therefore, only Fe-OOH nanoclusters and the ferrihydrite-like thin layers (1−3 nm) will allow the sufficient electron transport needed for the reduction of chemisorbed CO_2 species, as manifested by structural dynamics induced by the potential. It is also apparent that only a limited number of active centers in the Fe oxyhydroxide phase can chemisorb CO_2 and thus result in electron transfer, the first step toward CO_2 reduction. Most likely, these active centers are tetrahedral iron sites, as shown by the Fe L-edge spectra.

We also investigated the samples by NEXAFS at the N K-edge in UHV and under electrochemical polarization in Supplementary Figures S17a and S17b for FeOOH/OC and FeOOH/NC, respectively. The N K-edge spectra for these samples are characterized by a broad σ^* resonance at 409 eV that was suggested to be an interstitial N atom in the sp^3 bonding configuration, substituting an O atom in the Fe oxyhydroxide phase.[41] These nitrogen species in the fresh samples are derived from some residual N impurities due to the use of iron nitrate as a precursor to prepare the Fe oxyhydroxide phase. Compared to the spectra under UHV conditions, the N K-edge spectra of both samples measured at −0.3 V vs Ag/AgCl show the sharp resonance of molecular NO_x species at approximately 405 eV, while the main resonance is downshifted. The detailed analysis of these spectra is beyond the scope of this work, yet we note that the hydrolysis of these N impurities to form NO_x moieties[70] generates undercoordinated Fe atoms, which are the sites available for CO_2 chemisorption. The broad feature between 410 and 420 eV that appeared in the NK edge spectra of the electrocatalyst under *in situ* conditions was also observed for diamine-appended metal−organic frameworks upon the insertion of CO_2 into the Mg−N bond.[71]

The adsorption of CO_2 was confirmed in the case of FeOOH/NC in the C K-edge NEXAFS spectra (Supplementary Figure S18b). Particularly, we observed a resonance at an excitation energy of ∼286.5 eV, which was previously reported for adsorbed CO.[35] Indeed, the oxidation of the few Fe(II) sites could corroborate the dissociative chemisorption of CO_2 on reduced Fe(II). The amount of CO chemisorbed is significantly lower on FeOOH/OC (Supplementary Figure S18a), which is in agreement with the data on the electrocatalytic reactivity (Figure 4a) that show a lower efficiency toward carbon dioxide reduction.

Theoretical Modeling. Theoretical simulations were performed to elucidate binding geometries and strengths of CO_2 on the Fe oxyhydroxide phase and the bare NC support. Note that these results do not consider a wet surface and the presence of an applied potential.[72] Nevertheless, our simulations provide crucial information on the modalities of the chemisorption of CO_2 and the formation of isopropanol on Fe oxyhydroxide phases for the gas-phase CO_2RR. As shown in Figure 7a, while the CO_2 molecule only physisorbs on the simulated pristine NC (E_{Ads} = −0.14 eV), it chemisorbs and activates on FeOOH (E_{Ads} = −0.56 eV).

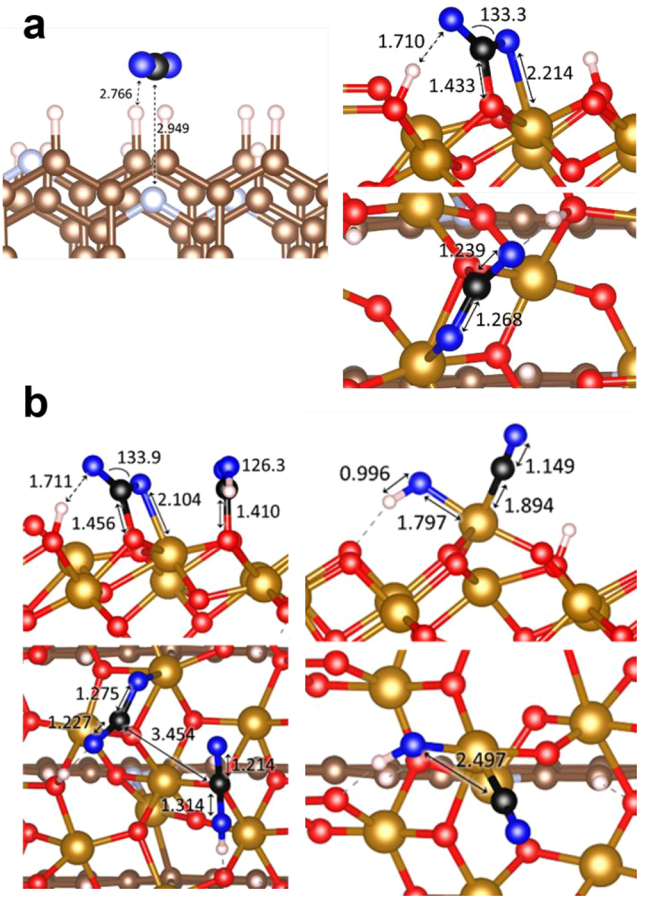

Figure 7. Rationalization of the C−C mechanism over thin-layer ferrihydrite via a computational analysis of the carbon dioxide adsorption geometry. (a) Schematic representation of (left) CO_2 physisorption on pristine NC and (right) CO_2 chemisorption on FeOOH/NC. The support color scheme for C, N, O, Fe, and H is brown, light blue, red, dark yellow, and white, respectively. For better distinction, C is black and O is blue in the CO_2 molecule. All distances and angles are in angstroms and degrees, respectively. (b) Schematic representations of (left) two coadsorbed molecules of CO_2 and (right) dissociated CO_2 on FeOOH/NC. The support color scheme for C, N, O, Fe, and H is brown, blue, red, dark yellow, and white, respectively. The CO_2 molecule is black and blue. All distances and angles are in angstroms and degrees respectively.

The chemisorption was confirmed both by the small surface-to-adsorbate distance and the elongated C−O bonds within the CO_2 molecule due to electrons being transferred to its antibonding orbital.[53] This ability of FeOOH to activate CO_2 likely explains its catalytic activity for CO_2RR. After activation and under AN external reduction potential, CO_2 dissociates and hydrogenates, leading to the chemisorbed intermediate species, *e.g.*, CO, that was observed experimentally.[32] The

https://doi.org/10.1021/acscatal.1c04296
ACS Catal. 2022, 12, 411−430

complete reduction of such species yields adsorbed C, promoting the formation of interstitial C.

Figure 7b indicates a distance of 3.454 Å between two adsorbed CO_2 groups. During the electrochemical process, reduced species sitting in such active sites are close enough to interact and form C−C bonds, yielding C_{2+} products.

We performed a series of calculations to validate the presence of C atoms on the FeOOH surface, as adsorbed CO may undergo further reduction to generate another H_2O molecule. In the first instance, forming a C adatom perpendicular the FeOOH surface is rather unfavorable ($CO^* + 2[H^+ + e^-] \rightarrow C^* + H_2O$; ΔE = 1.5 eV); however, the FeOOH is dynamic and may accommodate C within the lattice (Figure 8). The CO reduction leading to C in the

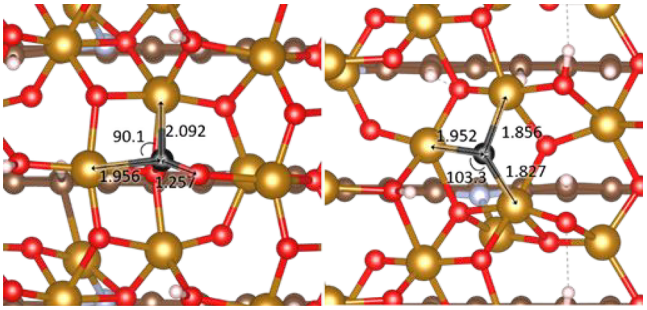

Figure 8. Top-view schematic representation of (left) a C adatom (black) within the FeOOH lattice and (right) a C atom (black) replacing an O atom in FeOOH. Inset values indicate distances and angles in angstroms and degrees. The support color scheme for C, N, O, Fe, and H are brown, light blue, red, dark yellow, and white, respectively.

FeOOH lattice (ΔE = 0.75 eV) may take place under moderate reduction. The formation of a lattice C atom is far more feasible, and exothermic, when it occupies an oxygen vacancy (ΔE = −1.29 eV), *e.g.*, under reductive conditions, FeOOH may establish an equilibrium between its reduced form and water molecules in the solution. Hence, the aliphatic fragment may adopt different length and conformations when the concentration of C species on the FeOOH surface increases.

We investigated the mechanism leading to *n*-propanol and isopropanol. The left-hand side of Figure 9 shows both product relative energies and, toward the right, intermediate species adsorbed on FeOOH/NC. The energies are relative to isolated reactants balanced with the number of water molecules yielded upon CO_2 reduction, *i.e.*, $3E_{CO_2} + 18/2E_{H_2} - 5E_{H_2O}$. The CO_2 reduction into methanol is driven by the exothermic formation of water molecules. The thermodynamic profiles indicate a preferential reduction of terminal methyl groups, as shown by the high relative energies of intermediates *i*-**1b**, *n*-**2b**, and *n*-**2c** in Figure 9 for the pathways toward isopropanol and *n*-propanol. The FeOOH/NC selectivity to form isopropanol across the *n*/*i* competitive route is determined by the higher stability of intermediates toward isopropanol, as shown by the relative energy of i-**1a** versus that of n-**1a**. Namely, intermediates n-**2c**, n-**2b**, and *i*-**1b** are accessible at higher energies than the low-energy pathway, which moves from *n*-**2a** to *n*-**1a** and to *n*-propanoate before desorbing as *n*-propanol.

Postulated Model of the Active Site and Mechanism. The results of the surface-sensitive APXPS and the more bulk-sensitive NEXAFS *in situ* measurements under polarization and

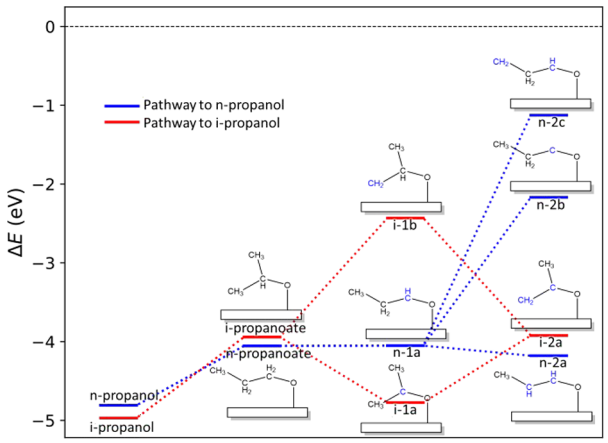

Figure 9. Relative thermodynamic energy profile for the formation of propanol and isopropanol from their deprotonated form. The different dotted lines indicate the formation paths to propanoate (blue line) and isopropanoate (red line). The bold group in the inset schematic representation of each intermediate indicates the changes (reduction) to the following structure in the reaction path, *i.e.*, right to left.

the controlled CO_2 + H_2O feed together with electron microscopy, electrocatalytic and cyclic voltammetry tests, and theory provide new insights into the dynamics of polarized FeOOH supported on N-doped carbon and the mechanisms of the conversion of CO_2 into C_3 products. Although these two aspects are strictly related, we discuss them separately for the sake of clarity.

Doping the carbon support with N creates a ferrihydrite-like catalyst with a productivity to isopropanol about one order of magnitude higher than the productivity obtained in the case of the O−C support. This enhanced productivity is also shown in the large increase of the carbon Faradaic efficiency to isopropanol (*i.e.*, with respect to CO_2 reduction products), which reaches over 90% for FeOOH/NC. To understand the role of the N-functionalization of the support, we should consider the coexistence of large ferrihydrite-like NPs and thin ferrihydrite layers as well as single atoms. These ferrihydrite layers are quasi-2D nanostructures and directly interact with the edges of the graphitic support where functional groups are present (Figure 3d−g).

As shown by the *in situ* spectroscopic data, only a fraction of the Fe phase is actually responsive to the electrode potential, and this fraction accounts for low-nuclearity Fe species and thin films. This fractional response can be explained by the poor conductivity of large particles of the ferrihydrite phase; moreover, one should consider the anisotropic character of graphite that also manifests in the directionality of electron conduction. In order for electron tunnelling from the support to the Fe phase bearing CO_2 species to occur, the interaction of the latter with the edge of the graphene layers must exist.

We can thus conclude that N-doping enables stronger bonds between the thin FeOOH species and the edge planes, which are the most electroactive species in our reaction conditions, *i.e.*, the gas-phase CO_2RR under the experimental conditions investigated here corresponding to the condition of highest isopropanol selectivity. We indeed observe that FeOOH/NC enables reduced Fe(II) species[6,41] that were predicted to occur due to the interaction with the N sites and were not observed for FeOOH/OC.

https://doi.org/10.1021/acscatal.1c04296
ACS Catal. 2022, 12, 411−430

The N-functionalization influences the hydrophobic or hydrophilic character of the carbon surface, which in turn influences the short- and long-range dispersive interactions, with the reagents modulating the proton availability. These interactions are particularly beneficial for reducing the surface coverage by excessive water in favor of the adsorption of CO_2 molecules and explain both the different behavior between different experiments on chemically identical FeOOH/NC and the improved performance of this sample compared to that of FeOOH/OC (Figure 4e and f and Supplementary Figure S14a).

The O 1s core level spectra for FeOOH/NC upon polarization are dominated by OH and C−O species (Figure 6c). The predominant effect we observe at a more negative potential, when CO_2 reduction occurs, is a reduction of the C═O chemisorbed on the metal species (part of the O3 component in Figure 6c), which is accompanied by the increase in the amount of the component assigned to the Fe−C species of interstitial or weakly bound atomic C in the Fe phase in the most surface-sensitive experiment (Figures 5b and 6a).[63−65,73] The amounts of other more electron-deficient CO species (part of the higher BE species in Figure 6c) increase as the potential decreases but are related to chemisorbed species due to capacitive processes on larger particles. The NEXAFS data show changes in the symmetry of the Fe sites (Fe L-edge NEXAFS in Supplementary Figure S16) induced by the hydrolysis of Fe−O and Fe−N bonds with the formation of NO_x moieties (Supplementary Figure S17). We postulate that coordinatively unsaturated Fe species are then able to coordinate and dissociate CO_2 into CO, as seen in previous controlled experiments.[6]

We consider that isopropanol formation is favored on the thin ferrihydrite phases stabilized by the interaction with the N-doping centers of carbon graphitic edges. Based on the results gathered, we hypothesize that the role of the N species at the edges is to favor the interfacial electron transfer process through the thin quasi 2D ferrihydrite layer to the chemisorbed species.[74] As a consequence, these species determine the redox potential at which this process occurs.

Various studies[75−77] have indicated that atomically dispersed Fe(III) sites are efficient in the CO_2 electroreduction to CO. On the one hand, we did not observe CO formation during the catalytic testing (Figure 4a and Supplementary Figure S14b−d). On the other hand, it is unlikely that single sites would be able, per se, to catalyze a multielectron transfer reaction such as isopropanol production, *i.e.*, an $18e^-$ reduction of CO_2. In addition, during the *in situ* measurements reported in Figure 5a and b as well as those in Figure 6a, we note a very dynamic metal support interface where the abundance of the peripheral C atoms of the graphene layers increases significantly as a consequence of the applied potential (due to both the CV and the subsequent CA).

Thus, we expect some mobility of the Fe single atoms to form clusters. We can focus the discussion on Fe−OOH nanoclusters and ferrihydrite-like thin layers, both of which sit at defective or edge sites of the graphitic support. These could be considered equivalent in terms of their reaction mechanism. The surface atomic C-species observed by C 1s XPS at 283.6 eV, generated *in situ* from CO_2 or CO reduction, are mobile and dissolve into the Fe phase upon polarization for selective CO_2 reduction. According to the theoretical calculation, the C adatoms are formed from the reduction of CO surface species and, due to the geometrical constraints imposed by the ferrihydrite structure, get close in proximity to other C surface species, with their configuration favoring fast coupling reactions.

A competition between the dissolution of atomic C in the near-surface region, its hydrogenation at the surface, and its reaction with chemisorbed C species leads to the selective formation of isopropanol, which is aligned with the epitaxial FeOOH interface. The availability of protons and electrons will determine the rates of hydrogenation and desorption of these intermediates versus the possibility of forming heavier products. A simplified model of the electroactive sites and the mechanism of C_3 product formation in FeOOH/NC is presented in Supplementary Scheme S1 in the Supporting Information.

Water acts not only as a competitive chemisorption species but also as a competitive species for electron transfer, which is a limiting factor in the behavior of these supported FeOOH. Thus, a gas-phase approach as in CO_2GR allows the provision of water to be limited, thus favoring the formation of multicarbon species.[29−31,79] This multicarbon selectivity is possible by controlling the potential to limit side reactions of protons or electron recombination and, at the same time, to avoid the excessive reduction of the FeOOH, which would lead to a selective state for the HER. We also consider that the extent of the dissolution of atomic C should be limited to the topmost atomic layers of the Fe phase to prevent the formation of a more stable carbide, which would be active for the HER.[78] A partially reduced thin layer of Fe(II) oxide in which lattice O atoms coexists with C atoms is an ideal phase where the N functionalization plays a crucial role in both stabilizing this structure and preventing phase transformation into HER active phases. Our experimental observations agree with a recent theoretical mechanistic study invoking atomic C in the formation of C_3 products.[80] Note that when a liquid electrolyte is in contact with the electrocatalyst (as in most of the contribution in the literature), a different mechanism may be possible. There, the larger availability of protons and water molecules explains the selectivity to acetic acid observed for the chemically identical systems in ref 6.

CONCLUSION

An *in situ* APXPS and NEXAFS study of the structural dynamics of carbon-supported FeOOH electrocatalysts in combination with electrocatalytic reactivity, multilength-scale electron microscopy, and theoretical modeling provides new insights into the gas-phase selective reduction of CO_2 to C_3 species (isopropanol). These gas-phase operations allow us to maximize the formation of C_{2+} products.

We discovered a new mechanism of formation for C_3 products on the Fe-phase, which involves the intermediate formation of atomic C due to the ability of Fe to dissolve interstitial C. The mechanism is effective only over few-layer FeOOH species, while thicker ferrihydrite-like nanoparticles remain largely inactive.

With respect to the three initial questions posed in the introduction, these results indicate a series of novel aspects regarding the factors responsible for the formation of C_{2+} products in the electrocatalytic reduction of CO_2:

1. Not only metallic Cu but also thin oxide films on a conductive support form a C_{2+} product.
2. A more complex mechanism than surface coupling of chemisorbed species, which involves the near-surface

https://doi.org/10.1021/acscatal.1c04296
ACS Catal. 2022, 12, 411−430

region of the electrode and its ability to host heteroatoms, leads to C_{2+} products.

3. Factors other than nanoconfinement, surface strains, and presence of tightly coupled atoms may lead to the formation C_{2+} products, such as controlling the availability of reactants via a dispersive interaction involving support surface chemistry.

These results describe a new chemistry for the synthesis of long-chain organic molecules, which had not yet been disclosed. We suggest that other elements able to dissolve C atoms could be used to obtain longer chain hydrocarbons under modulated experimental conditions that favor their subsequent hydrogenation at the expenses of stable carbide forms.

■ ASSOCIATED CONTENT

Supporting Information

The Supporting Information is available free of charge at https://pubs.acs.org/doi/10.1021/acscatal.1c04296.

Experimental conditions and additional results (PDF)

■ AUTHOR INFORMATION

Corresponding Authors

Rosa Arrigo − *School of Science, Engineering and Environment, University of Salford, Greater Manchester M5 4WT, U.K.; Diamond Light Source Ltd., Didcot, Oxfordshire OX11 0DE, U.K.;* orcid.org/0000-0002-2877-8733; Email: r.arrigo@salford.ac.uk

Alberto Roldan − *Cardiff Catalysis Institute, School of Chemistry, Cardiff University, Cardiff CF10 3AT Wales, U.K.;* orcid.org/0000-0003-0353-9004; Email: roldanmartineza@cardiff.ac.uk

Authors

Raoul Blume − *Department of Inorganic Chemistry, Fritz-Haber-Institut der Max-Planck Gesellschaft, 14195 Berlin, Germany; Max-Planck-Institut für Chemische Energiekonversion, 45470 Mülheim an der Ruhr, Germany*

Verena Streibel − *Department of Inorganic Chemistry, Fritz-Haber-Institut der Max-Planck Gesellschaft, 14195 Berlin, Germany;* orcid.org/0000-0002-7758-8610

Chiara Genovese − *Departments ChiBioFarAm, ERIC aisbl, and CASPE/INSTM, University of Messina, 98166 Messina, Italy*

Manfred E. Schuster − *Johnson Matthey Technology Centre, Reading RG4 9NH, U.K.*

Claudio Ampelli − *Departments ChiBioFarAm, ERIC aisbl, and CASPE/INSTM, University of Messina, 98166 Messina, Italy*

Siglinda Perathoner − *Departments ChiBioFarAm, ERIC aisbl, and CASPE/INSTM, University of Messina, 98166 Messina, Italy;* orcid.org/0000-0001-8814-1972

Juan J. Velasco Vélez − *Department of Inorganic Chemistry, Fritz-Haber-Institut der Max-Planck Gesellschaft, 14195 Berlin, Germany; Max-Planck-Institut für Chemische Energiekonversion, 45470 Mülheim an der Ruhr, Germany;* orcid.org/0000-0002-6595-0168

Michael Hävecker − *Department of Inorganic Chemistry, Fritz-Haber-Institut der Max-Planck Gesellschaft, 14195 Berlin, Germany; Max-Planck-Institut für Chemische Energiekonversion, 45470 Mülheim an der Ruhr, Germany*

Axel Knop-Gericke − *Department of Inorganic Chemistry, Fritz-Haber-Institut der Max-Planck Gesellschaft, 14195 Berlin, Germany; Max-Planck-Institut für Chemische Energiekonversion, 45470 Mülheim an der Ruhr, Germany*

Robert Schlögl − *Department of Inorganic Chemistry, Fritz-Haber-Institut der Max-Planck Gesellschaft, 14195 Berlin, Germany; Max-Planck-Institut für Chemische Energiekonversion, 45470 Mülheim an der Ruhr, Germany*

Gabriele Centi − *Departments ChiBioFarAm, ERIC aisbl, and CASPE/INSTM, University of Messina, 98166 Messina, Italy;* orcid.org/0000-0001-5626-9840

Complete contact information is available at: https://pubs.acs.org/10.1021/acscatal.1c04296

Author Contributions

R.A. conceived of and supervised the study. R.A., V.S., J.J.V.J., and M.H. measured *in situ* data. M.E.S. executed the TEM experiments and evaluated the data. R.A. and R.B. analyzed the *in situ* spectroscopic data. C.G. and C.A. measured reactivity data. A.R. carried out computational studies. R.A. and G.C. drafted and finalized the manuscript. S.P., A.K.-G, M.H., and R.S. gave general advisory both during the study and for finalizing the manuscript.

Notes

The authors declare no competing financial interest.

■ ACKNOWLEDGMENTS

The authors would like to acknowledge Dr. Panayiotis Tsaousis and Dr. Chanan Euaruksakul for support during beamtime. Measurements were carried out at the ISISS beamline at Helmholtz-Zentrum Berlin für Materialien und Energie. We thank HZB for the allocation of synchrotron radiation beamtime under the proposal ST 15202970. The research leading to the *in situ* spectroscopic results has been supported by the project CALIPSOplus under Grant 730872 from the EU Framework Programme for Research and Innovation HORIZON 2020. A.R. acknowledges the UK Centre for Circular Chemical Economy (EP/V011863/1). We also acknowledge computing time at the facilities of Supercomputing Wales and the Advanced Research Computing at Cardiff (ARCCA) at Cardiff University. R.A. acknowledges The UK Catalysis Hub for support provided via the membership of the UK Catalysis Hub Consortium, funded by EPSRC (portfolio Grants EP/K014706/1, EP/K014668/1, EP/K014854/1, EP/K014714/1, and EP/I019693/1).

■ REFERENCES

(1) Centi, G.; Perathoner, S. Catalysis for solar-driven chemistry: The role of electrocatalysis. *Catal. Today* **2019**, *330*, 157−170.

(2) Birdja, Y. Y.; Pérez-Gallent, E.; Figueiredo, M. C.; Göttle, A. J.; Calle-Vallejo, F.; Koper, M. T. M. Advances and challenges in understanding the electrocatalytic conversion of carbon dioxide to fuels. *Nature Energy* **2019**, *4*, 732−745.

(3) Kuhl, K. P.; Cave, E. R.; Abram, D. N.; Jaramillo, T. F. New insights into the electrochemical reduction of carbon dioxide on metallic copper surfaces. *Energy Environ. Sci.* **2012**, *5*, 7050−7059.

(4) Ampelli, C.; Genovese, C.; Marepally, B. C.; Papanikolaou, G.; Perathoner, S.; Centi, G. Electrocatalytic conversion of CO2 to produce solar fuels in electrolyte or electrolyte-less configurations of PEC cells. *Faraday Discuss.* **2015**, *183*, 125−145.

(5) Genovese, C.; Ampelli, C.; Perathoner, S.; Centi, G. Electrocatalytic conversion of CO2 on carbon nanotube-based electrodes for producing solar fuels. *J. Catal.* **2013**, *308*, 237−249.

(6) Genovese, C.; Schuster, M. E.; Gibson, E. K.; Gianolio, D.; Posligua, V.; Grau-Crespo, R.; Cibin, G.; Wells, P. P.; Garai, D.; Solokha, V.; Krick Calderon, S.; Velasco Velez, J.; Ampelli, C.; Perathoner, S.; Held, G.; Centi, G.; Arrigo, R. Operando spectroscopy study of the carbon dioxide electro-reduction by iron species on nitrogen-doped carbon. *Nat. Commun.* **2018**, *9*, 935.
(7) Marepally, B. C.; Ampelli, C.; Genovese, C.; Saboo, T.; Perathoner, S.; Wisser, F. M.; Veyre, L.; Canivet, J.; Quadrelli, E. A.; Centi, G. Enhanced formation of > C1 Products in Electroreduction of CO2 by Adding a CO2 Adsorption Component to a Gas-Diffusion Layer-Type Catalytic Electrode. *ChemSusChem* **2017**, *10*, 4442−4446.
(8) Gattrell, M.; Gupta, N.; Co, A. Electrochemical reduction of CO2 to hydrocarbons to store renewable electrical energy and upgrade biogas. *Energy Convers. Manage.* **2007**, *48*, 1255−1265.
(9) (a) Li, J.; Xu, A.; Li, F.; Wang, Z.; Zou, C.; Gabardo, C. M.; Wang, Y.; Ozden, A.; Xu, Y.; Nam, D.-H.; Lum, Y.; Wicks, J.; Chen, B.; Wang, Z.; Chen, J.; Wen, Y.; Zhuang, T.; Luo, M.; Du, X.; Sham, T.-K.; Zhang, B.; Sargent, E. H.; Sinton, D. Enhanced multi-carbon alcohol electroproduction from CO via modulated hydrogen adsorption. *Nat. Commun.* **2020**, *11*, 3685. (b) Wang, X.; Wang, Z.; García de Arquer, F. P.; Dinh, C.-T.; Ozden, A.; Li, Y. C.; Nam, D.-H.; Li, J.; Liu, Y.-S.; Wicks, J.; Chen, Z.; Chi, M.; Chen, B.; Wang, Y.; Tam, J.; Howe, J. Y.; Proppe, A.; Todorović, P.; Li, F.; Zhuang, T.-T.; Gabardo, C. M.; Kirmani, A. R.; McCallum, C.; Hung, S.-F.; Lum, Y.; Luo, M.; Min, Y.; Xu, A.; O'Brien, C. P.; Stephen, B.; Sun, B.; Ip, A. H.; Richter, L. J.; Kelley, S. O.; Sinton, D.; Sargent, E. H. Efficient electrically powered CO2-to-ethanol via suppression of deoxygenation. *Nat. Energy* **2020**, *5*, 478−486. (c) Li, J.; Che, F.; Pang, Y.; Zou, C.; Howe, J. Y.; Burdyny, T.; Edwards, J. P.; Wang, Y.; Li, F.; Wang, Z.; De Luna, P.; Dinh, C.-T.; Zhuang, T.-T.; Saidaminov, M. I.; Cheng, S.; Wu, T.; Finfrock, Y. Z.; Ma, L.; Hsieh, S.-H.; Liu, Y.-S.; Botton, G. A.; Pong, W.-F.; Du, X.; Guo, J.; Sham, T.-K.; Sargent, E. H.; Sinton, D. Copper adparticle enabled selective electrosynthesis of n-propanol. *Nat. Commun.* **2018**, *9*, 4614.
(10) (a) Velasco-Vélez, J.-J.; Jones, T.; Gao, D.; Carbonio, E.; Arrigo, R.; Hsu, C.-J.; Huang, Y.-C.; Dong, C.-L.; Chen, J.-M.; Lee, J.-F.; Strasser, P.; Roldan Cuenya, B.; Schlögl, R.; Knop-Gericke, A.; Chuang, C.-H. The Role of the Copper Oxidation State in the Electrocatalytic Reduction of CO_2 into Valuable Hydrocarbons. *ACS Sustainable Chem. Eng.* **2019**, *7*, 1485−1492. (b) Velasco-Vélez, J.-J.; Mom, R.; Sandoval-Diaz, L.-E.; Falling, L. J.; Chuang, C.-H.; Gao, D.; Jones, T.; Zhu, Q.; Arrigo, R.; Roldan Cuenya, B.; Knop-Gericke, A.; Lunkenbein, T.; Schlögl, R. Revealing the Active Phase of Copper during the Electroreduction of CO2 in Aqueous Electrolyte by Correlating In Situ X-ray Spectroscopy and In Situ Electron Microscopy. *ACS Energy Lett.* **2020**, *5*, 2106−2111. (c) Velasco-Vélez, J.-J.; Chuang, C.-H.; Gao, D.; Zhu, Q.; Ivanov, D.; Jeon, H. S.; Arrigo, R.; Mom, R. V.; Stotz, E.; Wu, H. L.; Jones, T. E.; Roldan Cuenya, B.; Knop-Gericke, A.; Schlögl, R. On the Activity/Selectivity and Phase Stability of Thermally Grown Copper Oxides during the Electrocatalytic Reduction of CO2. *ACS Catal.* **2020**, *10*, 11510−11518. (d) Eilert, A.; Roberts, F. S.; Friebel, D.; Nilsson, A. Formation of Copper Catalysts for CO2 Reduction with High Ethylene/Methane Product Ratio Investigated with In Situ X-ray Absorption Spectroscopy. *J. Phys. Chem. Lett.* **2016**, *7*, 1466−1470.
(11) Goodpaster, J. D.; Bell, A. T.; Head-Gordon, M. Identification of Possible Pathways for C-C Bond Formation during Electrochemical Reduction of CO2: New Theoretical Insights from an Improved Electrochemical Model. *J. Phys. Chem. Lett.* **2016**, *7*, 1471−1477.
(12) Gao, D.; Zegkinoglou, I.; Divins, N. J.; Scholten, F.; Sinev, I.; Grosse, P.; Roldan Cuenya, B. Plasma-Activated Copper Nanocube Catalysts for Efficient Carbon Dioxide Electroreduction to Hydrocarbons and Alcohols. *ACS Nano* **2017**, *11*, 4825−4831.
(13) Chang, X.; Malkani, A.; Yang, X.; Xu, B. Mechanistic insights into electroreductive C-C coupling between CO and acetaldehyde into multicarbon products. *J. Am. Chem. Soc.* **2020**, *142*, 2975−2983.
(14) Munir, S.; Varzeghani, A. R.; Kaya, S. Electrocatalytic reduction of CO2 to produce higher alcohols. *Energy Fuels* **2018**, *2*, 2532−2541.
(15) Li, Y.; Kim, D.; Louisia, S.; Xie, C.; Kong, Q.; Yu, S.; Lin, T.; Aloni, S.; Fakra, S. C.; Yang, P. Electrochemically scrambled nanocrystals are catalytically active for CO2-to-multicarbons. *Proc. Natl. Acad. Sci. U. S. A.* **2020**, *117*, 9194−9201.
(16) Zhuang, T.-T.; Pang, Y.; Liang, Z.-Q.; Wang, Z.; Li, Y.; Tan, C.-S.; Li, J.; Dinh, C. T.; De Luna, P.; Hsieh, P.-L.; Burdyny, T.; Li, H. H.; Liu, M.; Wang, Y.; Li, F.; Proppe, A.; Johnston, A.; Nam, D. H.; Wu, Z.-Y.; Zheng, Y.-R.; Ip, A. H.; Tan, H.; Chen, L.-J.; Yu, S.-H.; Kelley, S. O.; Sinton, D.; Sargent, E. H. Copper nanocavities confine intermediates for efficient electrosynthesis of C3 alcohol fuels from carbon monoxide. *Nat. Catal.* **2018**, *1*, 946−951.
(17) Zhang, B.-B.; Wang, Y.-H.; Xu, S.-M.; Chen, K.; Yang, Y.-G.; Kong, Q.-H. Tuning nanocavities of Au@Cu2O yolk−shell nanoparticles for highly selective electroreduction of CO2 to ethanol at low potential. *RSC Adv.* **2020**, *10*, 19192−19198.
(18) Sen, S.; Liu, D.; Palmore, G. T. R. Electrochemical Reduction of CO2 at Copper Nanofoams. *ACS Catal.* **2014**, *4*, 3091−3095.
(19) Lum, Y.; Yue, B.; Lobaccaro, P.; Bell, A. T.; Ager, J. W. Optimizing C−C Coupling on Oxide-Derived Copper Catalysts for Electrochemical CO2 Reduction. *J. Phys. Chem. C* **2017**, *121*, 14191−14203.
(20) Genovese, C.; Ampelli, C.; Perathoner, S.; Centi, G. Mechanism of C−C bond formation in the electrocatalytic reduction of CO2 to acetic acid. A challenging reaction to use renewable energy with chemistry. *Green Chem.* **2017**, *19*, 2406−2415.
(21) Chan, Y.-T.; Huang, I.-S.; Tsai, M.-K. Enhancing C−C bond formation by surface strain: a computational investigation for C2 and C3 intermediate formation on strained Cu surfaces. *Phys. Chem. Chem. Phys.* **2019**, *21*, 22704−22710.
(22) Marepally, B. C.; Ampelli, C.; Genovese, C.; Tavella, F.; Quadrelli, E. A.; Perathoner, S.; Centi, G. Electrocatalytic reduction of CO2 over dendritic-type Cu- and Fe-based electrodes prepared by electrodeposition. *J. CO2 Utiliz.* **2020**, *35*, 194−204.
(23) Han, H.; Noh, Y.; Kim, Y.; Park, S.; Yoon, W.; Jang, D.; Choi, S. M.; Kim, W. B. Selective electrochemical CO2 conversion to multicarbon alcohols on highly efficient N-doped porous carbon-supported Cu catalysts. *Green Chem.* **2020**, *22*, 71−84.
(24) Huang, Y.; Handoko, A. D.; Hirunsit, P.; Yeo, B. S. Electrochemical Reduction of CO2 Using Copper Single-Crystal Surfaces: Effects of CO* Coverage on the Selective Formation of Ethylene. *ACS Catal.* **2017**, *7*, 1749−1756.
(25) Schouten, K. J. P.; Qin, Z.; Gallent, E. P.; Koper, M. T. M. Two Pathways for the Formation of Ethylene in CO Reduction on Single-Crystal Copper Electrodes. *J. Am. Chem. Soc.* **2012**, *134*, 9864−9867.
(26) Montoya, J. H.; Shi, C.; Chan, K.; Nørskov, J. K. Theoretical Insights into a CO Dimerization Mechanism in CO2 Electroreduction. *J. Phys. Chem. Lett.* **2015**, *6*, 2032−2037.
(27) De Gregorio, G. L.; Burdyny, T.; Loiudice, A.; Iyengar, P.; Smith, W. A.; Buonsanti, R. Facet-Dependent Selectivity of Cu Catalysts in Electrochemical CO2 Reduction at Commercially Viable Current Densities. *ACS Catal.* **2020**, *10*, 4854−4862.
(28) Centi, G.; Perathoner, S.; Winè, G.; Gangeri, M. Electrocatalytic conversion of CO2 to long carbon-chain hydrocarbons. *Green Chem.* **2007**, *9*, 671−678.
(29) Arrigo, R.; Schuster, M. E.; Wrabetz, S.; Girgsdies, F.; Tessonnier, J.-P.; Centi, G.; Perathoner, S.; Su, D. S.; Schlögl, R. New insights from microcalorimetry on the FeOx/CNT-based electrocatalysts active in the conversion of CO2 to fuels. *ChemSusChem* **2012**, *5*, 577−586.
(30) (a) Perathoner, S.; Centi, G.; Su, D. S. Turning Perspective in Photoelectrocatalytic Cells for Solar Fuels. *ChemSusChem* **2016**, *9*, 345−357. (b) Ampelli, C.; Centi, G.; Passalacqua, R.; Perathoner, S. Electrolyte-less design of PEC cells for solar fuels: Prospects and open issues in the development of cells and related catalytic electrodes. *Catal. Today* **2016**, *259*, 246−258. (c) Garcia de Arquer, F. P.; Dinh, C.-T.; Ozden, A.; Wicks, J.; McCallum, C.; Kirmani, A. R.; Nam, D.-H.; Gabardo, C.; Seifitokaldani, A.; Wang, X.; Li, Y. C.; Li, F.; Edwards, J.; Richter, L. J.; Thorpe, S. J.; Sinton, D.; Sargent, E. H.

https://doi.org/10.1021/acscatal.1c04296
ACS Catal. 2022, 12, 411−430

CO_2 electrolysis to multicarbon products at activities greater than 1 A cm^{-2}. *Science* **2020**, *367*, 661−666.
(31) (a) Ampelli, C.; Genovese, C.; Errahali, M.; Gatti, G.; Marchese, L.; Perathoner, S.; Centi, G. CO2 capture and reduction to liquid fuels in a novel electrochemical setup by using metal-doped conjugated microporous polymers. *J. Appl. Electrochem.* **2015**, *45*, 701−713. (b) Gangeri, M.; Centi, G.; La Malfa, A.; Perathoner, S.; Vieira, R.; Pham-Huu, C.; Ledoux, M. J. Electrocatalytic performances of nanostructured platinum−carbon materials. *Catal. Today* **2005**, *102-103*, 50−57. (c) Gangeri, M.; Perathoner, S.; Caudo, S.; Centi, G.; Amadou, J.; Begin, D.; Pham-Huu, C.; Ledoux, M.J.; Tessonnier, J.-P.; Su, D.S. Fe and Pt carbon nanotubes for the electrocatalytic conversion of carbon dioxide to oxygenates. *Catal. Today* **2009**, *143*, 57−63.
(32) (a) Khatib, R.; Kumar, A.; Sanvito, S.; Sulpizi, M.; Cucinotta, C. S. The nanscale structure of the Pt-water double layer under bias revelead. *arXiv (Physics.Chemical Physics)*, May 28, **2019**, 1905.11850, ver. 1. https://arxiv.org/abs/1905.11850. (b) Mishra, A. K.; Roldan, A.; de Leeuw, N. H. A density functional theory study of the adsorption behaviour of CO_2 on Cu_2O surfaces. *J. Chem. Phys.* **2016**, *145*, 044709. (c) Roldan, A.; de Leeuw, N. H. *Faraday Discuss.* **2016**, *188*, 161−180.
(33) (a) Favaro, M.; Liu, Z.; Crumlin, E. J. Ambient-Pressure X-ray Photoelectron Spectroscopy to Characterize the Solid/Liquid Interface: Probing the Electrochemical Double Layer. *Synchrotron Radiation News* **2017**, *30*, 38−40. (b) Favaro, M.; Abdi, F. F.; Crumlin, E. J.; Liu, Z.; van de Krol, R.; Starr, D. E. Interface Science Using Ambient Pressure Hard X-ray Photoelectron Spectroscopy. *Surfaces* **2019**, *2*, 78−99.
(34) Held, G.; Venturini, F.; Grinter, D. C.; Ferrer, P.; Arrigo, R.; Deacon, L.; Quevedo Garzon, W.; Roy, K.; Large, A.; Stephens, C.; Watts, A.; Larkin, P.; Hand, M.; Wang, H.; Pratt, L.; Mudd, J. J.; Richardson, T.; Patel, S.; Hillman, M.; Scott, S. Ambient-pressure endstation of the Versatile Soft X-ray (VerSoX) beamline at Diamond Light Source. *J. Synchrotron Radiat.* **2020**, *27*, 1153−1166.
(35) Giorgianni, G.; Mebrahtu, C.; Schuster, M. E.; Large, A. I.; Held, G.; Ferrer, P.; Venturini, F.; Grinter, D.; Palkovits, R.; Perathoner, S.; Centi, G.; Abate, S.; Arrigo, R. Elucidating the mechanism of the CO2 methanation reaction over Ni−Fe hydrotalcite-derived catalysts via surface-sensitive in situ XPS and NEXAFS. *Phys. Chem. Chem. Phys.* **2020**, *22*, 18788−18797.
(36) (a) Streibel, V.; Havecker, M.; Yi, Y.; Velasco Velez, J. J.; Skorupska, K.; Stotz, E.; Knop-Gericke, A.; Schlogl, R.; Arrigo, R. In Situ Electrochemical Cells to Study the Oxygen Evolution Reaction by Near Ambient Pressure X-ray Photoelectron Spectroscopy. *Top. Catal.* **2018**, *61*, 2064−2084. (b) Arrigo, R.; Hävecker, M.; Schuster, M. E.; Ranjan, C.; Stotz, E.; Knop-Gericke, A.; Schlögl, R. In Situ Study of the Gas-Phase Electrolysis of Water on Platinum by NAP-XPS. *Angew. Chem., Int. Ed.* **2013**, *52*, 11660−11664.
(37) Knop-Gericke, A.; Pfeifer, V.; Velasco Vélez, J. J.; Jones, T. E.; Arrigo, R.; Hävecker, M.; Schlögl, R. In situ X-ray photoelectron spectroscopy of electrochemically active solid-gas and solid-liquid interfaces. *J. Electron Spectrosc. Relat. Phenom.* **2017**, *221*, 10−17.
(38) Law, Y. L.; Zafeiratos, S.; Neophytides, S. G.; Orfanidi, A.; Costa, D.; Dintzer, T.; Arrigo, R.; Knop-Gericke, A.; Schlögl, R.; Savinova, E. *In situ* investigation of dissociation and migration phenomena at the Pt/electrolyte interface of an electrochemical cell. *Chem. Science* **2015**, *6*, 5635−5642.
(39) Velasco-Velez, J.J.; Jones, T.E.; Streibel, V.; Havecker, M.; Chuang, C.-H.; Frevel, L.; Plodinec, M.; Centeno, A.; Zurutuza, A.; Wang, R.; Arrigo, R.; Mom, R.; Hofmann, S.; Schlögl, R.; Knop-Gericke, A. Electrochemically active Ir NPs on graphene for OER in acidic aqueous electrolyte investigated by in situ and ex situ spectroscopies. *Surf. Sci.* **2019**, *681*, 1−8.
(40) Toghan, A.; Arrigo, R.; Knop-Gericke, A.; Imbihl, R. Ambient pressure X-ray photoelectron spectroscopy during electrochemical promotion of ethylene oxidation over a bimetallic Pt−Ag/YSZ catalyst. *J. Catal.* **2012**, *296*, 99−109.
(41) Arrigo, R.; Schuster, M. E, On the High Structural Heterogeneity of Fe-Impregnated Graphitic-Carbon Catalysts from Fe Nitrate Precursor. *Catalysts* **2019**, *9*, 303.
(42) (a) Arrigo, R.; Haevecker, M.; Wrabetz, S.; Blume, R.; Lerch, M.; McGregor, J.; Parrott, E. P. J.; Zeitler, J. A.; Gladden, L. F.; Knop-Gericke, A.; Schloegl, R.; Su, D. S. Tuning the Acid/Base Properties of Nanocarbons by Functionalization via Amination. *J. Am. Chem. Soc.* **2010**, *132*, 9616−9630. (b) Arrigo, R. *Nitrogen Functionalization of CNFs and Application in Heterogeneous Catalysis*. Ph.D. Thesis, Fritz Haber Institute, Berlin, Germany, 2009. http://hdl.handle.net/11858/00-001M-0000-0010-F842-3.
(43) Arrigo, R.; Wrabetz, S.; Schuster, M. E.; Wang, D.; Villa, A.; Rosenthal, D.; Girsgdies, F.; Weinberg, G.; Prati, L.; Schlögl, R.; Su, D. S. Tailoring the morphology of Pd nanoparticles on CNTs by nitrogen and oxygen functionalization. *Phys. Chem. Chem. Phys.* **2012**, *14*, 10523−10532.
(44) Tessonnier, J. P.; Rosenthal, D.; Hansen, T. W.; Hess, C.; Schuster, M. E.; Blume, R.; Girgsdies, F.; Pfänder, N.; Timpe, O.; Su, D. S.; Schlögl, R. Analysis of the structure and chemical properties of some commercial carbon nanostructures. *Carbon* **2009**, *47*, 1779−1798.
(45) Friedel Ortega, K.; Arrigo, R.; Frank, B.; Schlögl, R.; Trunschke, A. Acid−Base Properties of N-Doped Carbon Nanotubes: A Combined Temperature-Programmed Desorption, X-ray Photoelectron Spectroscopy, and 2-Propanol Reaction Investigation. *Chem. Mater.* **2016**, *28*, 6826−6839.
(46) Doniach, S.; Sunjic, M. *J. Phys. C: Solid State Phys.* **1970**, *3*, 285−291.
(47) Shirley, D. A. High-Resolution X-Ray Photoemission Spectrum of the Valence Bands of Gold. *Phys. Rev. B* **1972**, *5*, 4709−4714.
(48) Blume, R.; Rosenthal, D.; Tessonnier, J.-P.; Li, H.; Knop-Gericke, A.; Schlögl, R. Characterizing Graphitic Carbon with X-ray Photoelectron Spectroscopy: A Step-by-Step Approach. *ChemCatChem* **2015**, *7*, 2871−2882.
(49) Biesinger, M. C.; Payne, B. P.; Grosvenor, A. P.; Lau, L. W.M.; Gerson, A. R.; Smart, R. St. C. Resolving surface chemical states in XPS analysis of first row transition metals, oxides and hydroxides: Cr, Mn, Fe, Co and Ni. *Appl. Surf. Sci.* **2011**, *257*, 2717−2730.
(50) (a) Frank, B.; Blume, R.; Rinaldi, A.; Trunschke, A.; Schloegl, R. Oxygen insertion catalysis by sp^2 carbon. *Angew. Chem., Int. Ed.* **2011**, *50*, 10226−10230. (b) Reiche, S.; Blume, R.; Zhao, X. C.; Su, D.; Kunkes, E.; Behrens, M.; Schlögl, R. Reactivity of mesoporous carbon against water − An in-situ XPS study. *Carbon* **2014**, *77*, 175−183.
(51) (a) Kresse, G.; Hafner, J. Ab initio molecular dynamics for liquid metals. *Phys. Rev. B: Condens. Matter Mater. Phys.* **1993**, *47*, 558−561. (b) Kresse, G.; Furthmüller, J. Efficient iterative schemes for ab initio total-energy calculations using a plane-wave basis set. *Phys. Rev. B: Condens. Matter Mater. Phys.* **1996**, *54*, 11169−11186. (c) Kresse, G.; Joubert, D. From ultrasoft pseudopotentials to the projector augmented-wave method. *Phys. Rev. B: Condens. Matter Mater. Phys.* **1999**, *59*, 1758−1775.
(52) Perdew, J. P.; Burke, K.; Ernzerhof, M. Generalized Gradient Approximation Made Simple. *Phys. Rev. Lett.* **1996**, *77*, 3865−3868.
(53) Roldan, A.; Hollingsworth, N.; Roffey, A.; Islam, H.-U.; Goodall, J. B. M.; Catlow, C. R. A.; Darr, J. A.; Bras, W.; Sankar, G.; Holt, K. B.; Hogarth, G.; de Leeuw, N. H. Bio-inspired CO2 conversion by iron sulfide catalysts under sustainable conditions. *Chem. Commun.* **2015**, *51*, 7501−7505.
(54) Puigdollers, A. R.; Schlexer, P.; Pacchioni, G. Gold and Silver Clusters on TiO2 and ZrO2 (101) Surfaces: Role of Dispersion Forces. *J. Phys. Chem. C* **2015**, *119*, 15381−15389.
(55) Zakaria, S.N. A.; Hollingsworth, N.; Islam, H. U.; Roffey, A.; Santos-Carballal, D.; Roldan, A.; Bras, W.; Sankar, G.; Hogarth, G.; Holt, K. B.; de Leeuw, N. H. Insight into the Nature of Iron Sulfide Surfaces During the Electrochemical Hydrogen Evolution and CO_2 Reduction Reactions. *ACS Appl. Mater. Interfaces* **2018**, *10*, 32078−32085.

https://doi.org/10.1021/acscatal.1c04296
ACS Catal. 2022, 12, 411−430

(56) Grimme, G.; Antony, J.; Ehrlich, S.; Krieg, H. A consistent and accurate *ab initio* parametrization of density functional dispersion correction (DFT-D) for the 94 elements H-Pu. *J. Chem. Phys.* **2010**, *132*, 154104.
(57) Blöchl, P. E. Projector augmented-wave method. *Phys. Rev. B: Condens. Matter Mater. Phys.* **1994**, *50*, 17953−17979.
(58) Bader, R. F. W. Atoms in molecules. *Acc. Chem. Res.* **1985**, *18*, 9−15.
(59) Michel, F. M.; Ehm, L.; Antao, S. M.; Lee, P. L.; Chupas, P. J.; Liu, G.; Strongin, D. R.; Schoonen, M. A. A.; Phillips, B. L.; Parise, J. B. The structure of ferrihydrite, a nanocrystalline material. *Science* **2007**, *316*, 1726−1729.
(60) (a) Brito, J. F.; Genovese, C.; Tavella, F.; Ampelli, C.; Boldrin Zanoni, M. V.; Centi, G.; Perathoner, S. CO_2 Reduction of Hybrid Cu_2O−Cu/Gas Diffusion Layer Electrodes and their Integration in a Cu-based Photoelectrocatalytic Cell. *ChemSusChem* **2019**, *12*, 4274−4284. (b) Ampelli, C.; Genovese, C.; Cosio, D.; Perathoner, S.; Centi, G. Effect of Current Density on Product Distribution for the Electrocatalytic Reduction of CO2. *Chem. Eng. Trans.* **2019**, *74*, 1285−1290.
(61) (a) Peng, C.; Luo, G.; Zhang, J.; Chen, M.; Wang, Z.; Sham, T.-K.; Zhang, L.; Li, Y.; Zheng, G. Double sulfur vacancies by lithium tuning enhance CO2 electroreduction to n-propanol. *Nat. Commun.* **2021**, *12*, 1580. (b) Han, Z.; Kortlever, R.; Chen, H.-Y.; Peters, J. C.; Agapie, T. CO2 Reduction Selective for C ≥ 2 Products on Polycrystalline Copper with N-Substituted Pyridinium Additives. *ACS Cent. Sci.* **2017**, *3*, 853−859. (c) Zhu, Q.; Sun, X.; Yang, D.; Ma, J.; Kang, X.; Zheng, L.; Zhang, J.; Wu, Z.; Han, B. Carbon dioxide electroreduction to C2 products over copper-cuprous oxide derived from electrosynthesized copper complex. *Nat. Commun.* **2019**, *10*, 3851.
(62) Bard, A.J.; Faulkner, L.R. *Electrochemical Methods: Fundamentals and Applications*, 2nd ed.; Wiley: New York, NY, 2000.
(63) Furlan, A.; Jansson, U.; Lu, J.; Hultman, L.; Magnuson, M. Structure and Bonding in Amorphous Iron Carbide Thin Films. *J. Phys.: Condens. Matter* **2015**, *27*, 045002.
(64) Weatherup, R. S.; Bayer, B. C.; Blume, R.; Baehtz, C.; Kidambi, P. R.; Fouquet, M.; Wirth, C. T.; Schlögl, R.; Hofmann, S. On the Mechanisms of Ni-Catalysed Graphene Chemical Vapour Deposition. *ChemPhysChem* **2012**, *13*, 2544−2549.
(65) Bayer, B. C.; Hofmann, S.; Castellarin-Cudia, C.; Blume, R.; Baehtz, C.; Esconjauregui, S.; Wirth, C. T.; Oliver, R. A.; Ducati, C.; Knop-Gericke, A.; Schlögl, R.; Goldoni, A.; Cepek, C.; Robertson, J. Support-Catalyst-Gas Interactions during Carbon Nanotube Growth on Metallic Ta Films. *J. Phys. Chem. C* **2011**, *115*, 4359−4369.
(66) Tanuma, S.; Powell, C. J.; Penn, D. R. Calculations of electron inelastic mean free paths. V. Data for 14 organic compounds over the 50−2000 eV range. *Surf. Interface Anal.* **1994**, *21*, 165−176.
(67) Peak, D.; Regier, T. Direct Observation of Tetrahedrally Coordinated Fe(III) in Ferrihydrite. *Environ. Sci. Technol.* **2012**, *46*, 3163−3168.
(68) Habib, K. Surface resistivity/conductivity of oxide−hydroxide compounds in inhibited seawater by optical interferometry. *J. Saudi Chem. Soc.* **2016**, *20*, S541−S546.
(69) Xia, Q.; Xu, M.; Xia, H.; Xie, J. Nanostructured Iron Oxide/Hydroxide-Based Electrode Materials for Supercapacitors. *ChemNanoMat* **2016**, *2*, 588−600.
(70) Křepelová, A.; Newberg, J.; Huthwelker, T.; Bluhm, H.; Ammann, M. The nature of nitrate at the ice surface studied by XPS and NEXAFS. *Phys. Chem. Chem. Phys.* **2010**, *12*, 8870−8880.
(71) McDonald, T.; Mason, J.; Kong, X.; Bloch, E. D.; Gygi, D.; Dani, A.; Crocellà, V.; Giordanino, F.; Odoh, S. O.; Drisdell, W. S.; Vlaisavljevich, B.; Dzubak, A. L.; Poloni, R.; Schnell, S. K.; Planas, N.; Lee, K.; Pascal, T.; Wan, L. F.; Prendergast, D.; Neaton, J. B.; Smit, B.; Kortright, J. B.; Gagliardi, L.; Bordiga, S.; Reimer, J. A.; Long, J. R. Cooperative insertion of CO2 in diamine-appended metal-organic frameworks. *Nature* **2015**, *519*, 303−308.
(72) Roldan, A. Frontiers in first principles modelling of electrochemical simulations. *Current Opinion in Electrochemistry* **2018**, *10*, 1−6.
(73) Rinaldi, A.; Tessonnier, J.-P.; Schuster, M. E.; Blume, R.; Girgsdies, F.; Zhang, Q.; Jacob, T.; Abd Hamid, S. B.; Su, D. S.; Schlögl, R. Dissolved Carbon Controls the Initial Stages of Nanocarbon Growth. *Angew. Chem., Int. Ed.* **2011**, *50*, 3313−3317.
(74) Pacchioni, G. Two-Dimensional Oxides and Their Role in Electron Transfer Mechanisms with Adsorbed Species. *Chem. Rec.* **2014**, *14*, 910−922.
(75) Gu, J.; Hsu, C.-S.; Bai, L.; Chen, H. M.; Hu, X. Atomically dispersed Fe3+ sites catalyze efficient CO2 electroreduction to CO. *Science* **2019**, *364*, 1091−1094.
(76) Zhang, H.; Li, J.; Xi, S.; Du, Y.; Hai, X.; Wang, J.; Xu, H.; Wu, G.; Zhang, J.; Lu, J.; Wang, J. A Graphene-Supported Single-Atom FeN5 Catalytic Site for Efficient Electrochemical CO2 Reduction. *Angew. Chem., Int. Ed.* **2019**, *58*, 14871−14876.
(77) (a) Pan, F.; Li, B.; Sarnello, E.; Fei, Y.; Gang, Y.; Xiang, X.; Du, Z.; Zhang, P.; Wang, G.; Nguyen, H. T.; Li, T.; Hu, Y. H.; Zhou, H.-C.; Li, Y. Atomically Dispersed Iron−Nitrogen Sites on Hierarchically Mesoporous Carbon Nanotube and Graphene Nanoribbon Networks for CO2 Reduction. *ACS Nano* **2020**, *14*, 5506−5516. (b) Su, D. S.; Perathoner, S.; Centi, G. Nanocarbons for the Development of Advanced Catalysts. *Chem. Rev.* **2013**, *113*, 5782−5816. (c) Xu, J.; Kan, Y.; Huang, R.; Zhang, B.; Wang, B.; Wu, K. H.; Lin, Y.; Sun, X.; Li, Q.; Centi, G.; Su, D. S. Revealing the Origin of Activity in Nitrogen-Doped Nanocarbons towards Electrocatalytic Reduction of Carbon Dioxide. *ChemSusChem* **2016**, *9*, 1085−1089.
(78) (a) Li, S.; Ren, P.; Yang, C.; Liu, X.; Yin, Z.; Li, W.; Yang, H.; Li, J.; Wang, X.; Wang, Y.; Cao, R.; Lin, L.; Yao, S.; Wen, X.; Ma, D. Fe5C2 nanoparticles as low-cost HER electrocatalyst: the importance of Co substitution. *Sci. Bull.* **2018**, *63*, 1358−1363. (b) Giordano, L.; Pacchioni, G., Unusual Properties of Oxides and Other Insulators in the Ultrathin Limit Oxide. In *Ultrathin Films: Science and Technology*; Wiley: Berlin, Germany, 2012.
(79) Giusi, D.; Ampelli, C.; Genovese, C.; Perathoner, S.; Centi, G. A novel gas flow-through photocatalytic reactor based on copper-functionalized nanomembranes for the photoreduction of CO2 to C1-C2 carboxylic acids and C1-C3 alcohols. *Chem. Eng. J.* **2021**, *408*, 127250−12.
(80) Peng, H.; Tang, M. T.; Liu, X.; Schlexer Lamoureux, P.; Bajdich, M.; Abild-Pedersen, F. The Role of Atomic Carbon in Directing Electrochemical $CO_{(2)}$ Reduction to Multicarbon Products. *Energy Environ. Sci.* **2021**, *14*, 473−482.

https://doi.org/10.1021/acscatal.1c04296
ACS Catal. 2022, 12, 411−430